


12-2012

Penetration Forces for Subsurface Regolith Probes

Ahmed Elshafie

University of Arkansas, Fayetteville

Follow this and additional works at: <http://scholarworks.uark.edu/etd>

 Part of the [Geology Commons](#), [Geomorphology Commons](#), [Stars, Interstellar Medium and the Galaxy Commons](#), and the [The Sun and the Solar System Commons](#)

Recommended Citation

Elshafie, Ahmed, "Penetration Forces for Subsurface Regolith Probes" (2012). *Theses and Dissertations*. 574.
<http://scholarworks.uark.edu/etd/574>

This Thesis is brought to you for free and open access by ScholarWorks@UARK. It has been accepted for inclusion in Theses and Dissertations by an authorized administrator of ScholarWorks@UARK. For more information, please contact scholar@uark.edu, ccmiddle@uark.edu.

PENETRATION FORCES FOR SUBSURFACE REGOLITH PROBES

PENETRATION FORCES FOR SUBSURFACE REGOLITH PROBES

A thesis submitted in partial fulfilment
of the requirements for the degree of
Master of Science in Space and Planetary Science

By

Ahmed Mohamed ElShafie
Cairo University
Bachelor of Space Science, 2005
University of Arkansas
Doctorate of Space and Planetary Science, 2012

December 2012
University of Arkansas

ABSTRACT

Investigating planetary bodies using penetrometers can provide detailed information about its history and evolution. An estimation of subsurface density and porosity can be made from the shape of the penetration curve. Using penetrometers mounted on planetary platforms could be challenging due to the uncertainty of the subsurface composition and since the maximum allowed force for penetration is the weight of the lander or rover on the surface. Estimation of penetration forces can provide a reliable constraint on the maximum reachable depth without endangering the whole mission. Therefore, knowledge of the required penetration force to specific depths can be helpful in designing the length and shape of the probe. Test probes covering the anticipated diameter (2.5, 1.9, 1.2 and 0.9 cm diameter) and tip angle (30°, 60°, 90° and 120°) were inserted mechanically into regolith analogs. The results showed that tip angle does not have a major effect, while probe diameter and density of the regolith are the most important parameters. Increasing probe diameter from 0.9 to 1.9 cm (i.e. a factor of 2) leads to an increase in penetration force from 200 to 1000 N (i.e. a factor of 5) at 20 cm depth. An increase in bulk density from 1550 to 1700 kg/m³ leads to an increase in penetration force from 10 to 200 N at 20 cm depth. Square probes required less force than circular ones which can allow for easier design of lateral windows.

This thesis is approved for Recommendation to the
Graduate Council

Thesis Director:

(Dr. Rick Ulrich)

Thesis Committee:

(Dr. Mark Arnold)

(Dr. Larry Roe)

(Dr. Claud Lacy)

THESIS DUPLICATION RELEASE

I hereby authorize the University of Arkansas Libraries to duplicate this Thesis when needed for research and/or scholarship.

Agreed _____

(Ahmed Mohamed ELShafie)

TABLE OF CONTENTS

1	Introduction.....	1
	1.1 Layers in the Solar System	2
2	The Optical Probe for Regolith Analysis	6
3	Literature Review	9
	3.1 Introduction	9
	3.2 Effects of Low Gravity Environment on Penetration	10
	3.3 Example of Dynamic Penetrometer (PLUTO mole)	11
	3.4 Penetration Testing on the Moon	14
4	Experimental Apparatus	16
5	Experimental Procedures	28
	5.1 Validation of the Force Sensor	28
	5.2 Loading of the Regolith Samples	29
	5.3 Penetration Probes	29
	5.4 Procedure for Conducting the Penetration Experiments	31
	5.5 Regolith Particles Size Distribution	31
6	Experimental Results	34
	6.1 Effect of Bulk Density	34
	6.2 Effect of Compaction	35
	6.3 Effect of Penetration Speed	37
	6.4 Effect of Tip Angle	38
	6.5 Effect of Cross Section Shape	43
	6.6 Effect of Diameter	50
7	Discussion	53
	7.1. Bearing Capacity Theory	53
	7.2. Procedure for determining q_c in sand	54
	7.3. Theoretical Vs Experimental data	57
8	Conclusions	60
9	References	62

1. Introduction

1.1. Layers in the Solar System

Planets formed as a result of accretion of small objects (planetesimals) that were condensed out of the solar nebula. The planets passed through four main processes starting from their formation to their current state:

- Differentiation - The separation of materials according to their density; dense materials sank down toward the planet's center and lighter materials floated towards the surface (Spencer, 1983).
- Bombardment - The surfaces of planets were impacted by asteroids and leftover planetesimals. This event lasted for several hundred million years and is the main cause of craters that are seen on planetary surfaces.
- Radioactive decay of elements - Heating from radiogenic decay produced subsurface lava that could reach the surface through fissures or craters punched by impacts. This lava flooded at least some surface areas of terrestrial planets.
- Surface evolution - Chemical and physical modification by atmospheric and fluvial processes (Strahler, 1981).

This planetary history can be revealed by studying the records that are preserved in the resulting geological formations. Layers in consolidated and unconsolidated materials are the pages of this history book. Younger layers formed on the top of older layers based on the principle of superposition. According to the law of original horizontality, each layer was formed

in a horizontal configuration due to gravitational effects but their orientation could have been modified by various processes that can result in uplifting and folding (Longwell and Flint, 1962).

Layering may be formed by several processes. Igneous layers are formed when lava flows over a surface and solidifies due to convective, conductive or radiative cooling. These layers begin as consolidated materials and are always solid in nature. Sedimentary layers are formed when unconsolidated material is transported by aeolian or fluvial means and deposited over a substrate of a different composition. Layers such as these may remain granular or may consolidate into a solid mass due to pressure, heat and/or chemical action. If deeply buried, either igneous or sedimentary layers can be acted upon by heat and pressure to the extent that the chemical bonding of their materials is changed, resulting in a layer of metamorphic rock. These layers would also be consolidated.

Layering has been observed on almost every solid body in the solar system with individual thicknesses from a few millimetres to hundreds of meters, and with bed depths up to kilometres in vertical extent. Layering on Earth is abundantly documented, of course, but layering has also been studied in various degrees of detail elsewhere. Sedimentary layers exist on Venus such as the 100,000 km² terminal deposits to the Kallistos Vallis channel (Jones & Pickering, 2003) and are also abundant on Mars. Figure 1.1 is a Mars Global Surveyor image of a 2.3 km impact crater in northwestern Schiaparelli Basin, revealing layers that are 10's to 100's of m thick. Figure 1.2 shows sedimentary layering in the Victoria crater ~750 m in diameter (Squyres et al., 2008)



Figure 1.1. Meteor impact crater in northwestern Schiaparelli basin (2.3 km in diameter) revealing extensive layering hundreds of meters below the surface (<http://photojournal.jpl.nasa.gov/catalog/pia04592>).

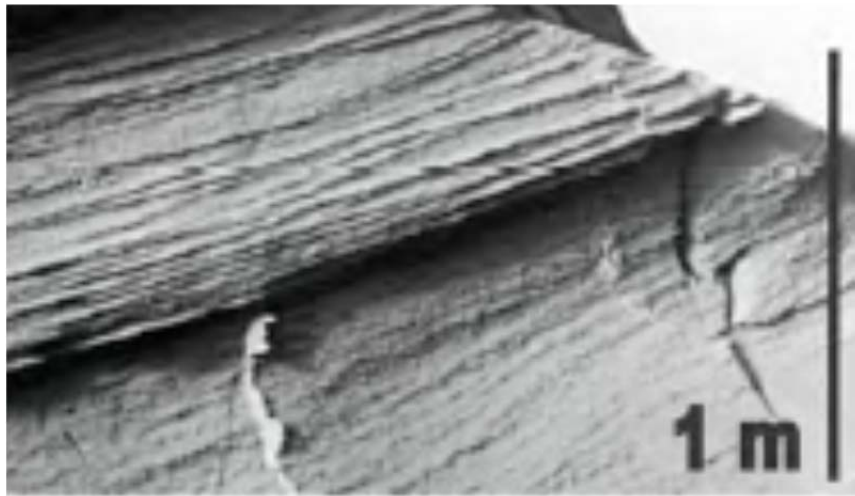


Figure 1.2. Layering in the Victoria crater ~750-meter in diameter (Squyre et al., 2008)

The presence of these sedimentary and erosion in Victoria crater is an indicative of a past dynamic environment.

Figure 1.3 shows the light-toned icy layer approximately 5 cm below the surface at the Phoenix landing site. This ice may be the remnants of past liquid water on Mars and may have locked within it preserved chemical and possibly biological samples from billions of years ago. Data from the gamma ray spectrometer on Mars Odyssey indicate that an ice layer just below the surface regolith is pervasive above about latitude 50° in both hemispheres.

Gullies on the sides of Martian craters are one of the most intensely studied features of that planet since they may indicate the presence of liquid water in geologically recent times. These gullies frequently originate from sedimentary layers as shown in Figure 1.4.

The motivation for this project is to address some of the engineering issues associated with the design and construction of instruments to study layers such as these on other planets, moons, asteroids and comets.



Figure 1.3. This image shows the subsurface layer of ice on Mars. Image taken by Phoenix lander on June 15, 2008. Image credit: NASA/JPL-Caltech/University of Arizona/Texas A&M University

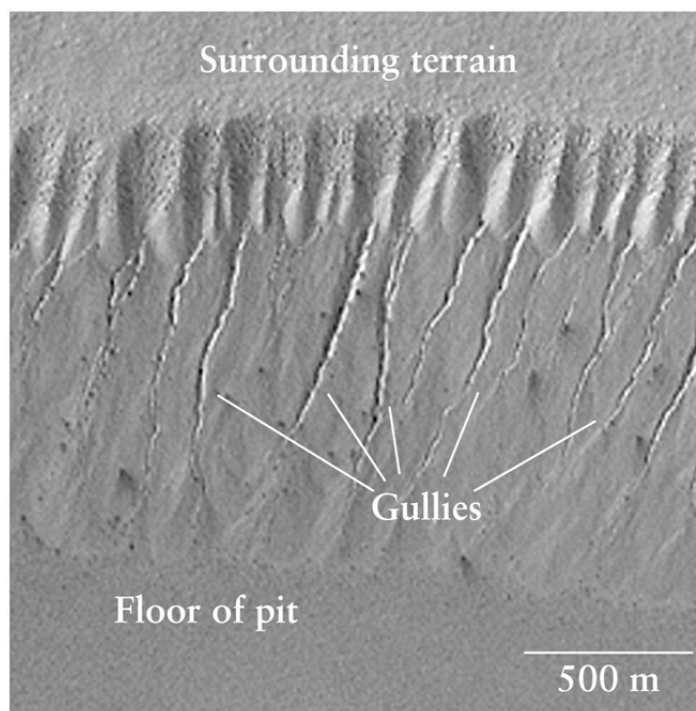


Figure 1.4. Gullies on Mars sometimes originate from layered deposits. <http://astroprofspage.com/archives/542>

2. The Optical Probe for Regolith Analysis (OPRA)

OPRA (Fig. 2.1) was envisioned as a probe with vertically-stacked windows that would be inserted from either a lander or rover into a regolith or unconsolidated ices on the surface of a planet, asteroid, moon or comet. These windows would be connected by fiber optics to an IR spectrometer located in the body of the spacecraft. The spectrometer will address each window individually, providing swept frequency illumination to subsurface material outside the window and simultaneously returning the reflected signal to the unit. The result would be a spectral composition profile of the surface material sampled at least every couple of cm's down to as much as a meter. If a borehole into consolidated material is available, OPRA could be inserted into there to provide a geochemical depth profile. Because the probe will be thin and since the heat-producing electronics are up in the spacecraft, disturbance of the subsurface layers should be minimal. There are no moving parts in the probe and all electronics may be located in the warm-box within the rover or spacecraft body. The spectral range will be 0.5 to 5 μm (20,000 – 2000 cm^{-1}) which is suitable for the mineralogical and chemical characterization of the subsurface. It also includes the water band at $\sim 3 \mu\text{m}$ and various ices.

OPRA will have the shape of penetrometer with windows placed laterally along the side (Fig. 2.2). These windows will protect the fiber optic cables from being in direct contact with subsurface material. Some fibers will carry illumination to the windows and others will carry the returning signal to the IR instrument. These fibers will be attached to the windows using optically transparent, non-outgassing epoxy, using aerospace-proven methods and materials. The number of windows is function of the probe's diameter, length and fiber optic diameter.

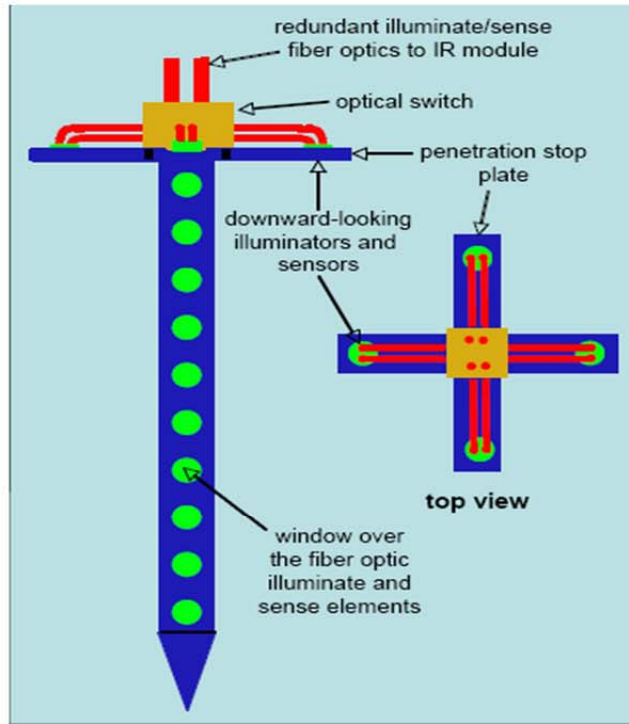


Figure 2.1. The Optical Probe for Regolith Analysis (OPRA).

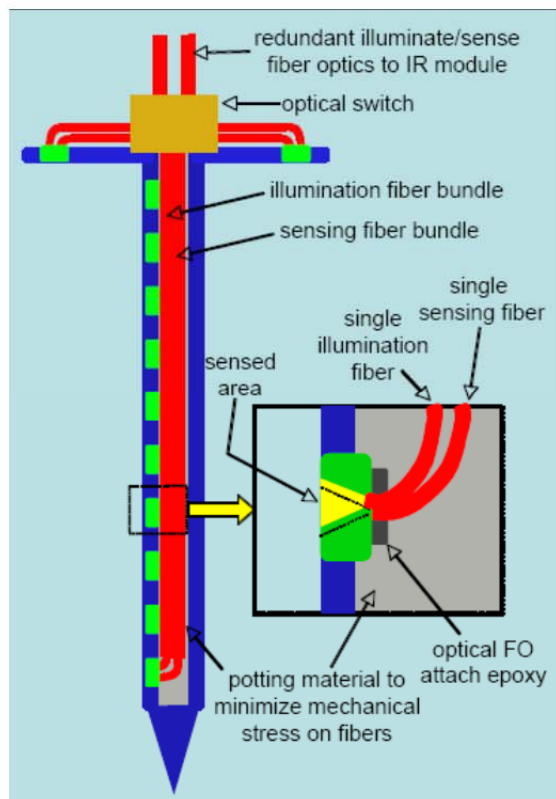


Figure 2.2. OPRA as a penetrometer-like shape with windows placed on the side.

There are two general tasks in the overall design of OPRA:

1) Design the Optical Train, Spectral Demonstration and Calibration

This will include the development of the optics at and near the windows and covered the required number of fiber optical cables needed to illuminate and receive illumination sufficient intensity, taking into account considerations of field of view and sampled area (Pilgrim and Ulrich, 2012). The conclusion of this investigation addressed the size of the windows and its thickness, diameter of the fibers and methods of attachment between the fibers and the windows. Spectra taken using FTIR spectrometer for various consolidated and unconsolidated minerals as well as water ice and icy soils will be helpful for calibration purposes before or during a mission.

2) Mechanical and Penetration Testing

Since OPRA is going to be a penetrometer, it will be crucial to know the force required to insert a probe in the subsurface and the corresponding withdrawal force both as a function of depth.

The main objective of this research involves the second task; the measurement of the amount of force needed to insert and withdraw different probes to and from the subsurface as a function of the probe's shape, length, weight, tip angle and penetration speed into various planetary analogs (JSC Mars-1, JSC Mars-2 and Mojave). The outcome of these experiments is to optimize the probe's configuration to minimum penetration force.

3. Literature Review

3.1. Introduction

Table 3.1 shows some of the various methods to deliver an instrument into the subsurface of planets, asteroids and comets for the purpose of studying geological layering.

Table 3.1. Various methods to access the subsurface of planetary bodies

Method	Description
Drill	Applies torque and axial force to break the formation and remove cuttings from the hole.
Penetrator/penetrometer	Applies axial force to compress and displace the formation and create a hole.
Hypervelocity Impactor	Strikes the surface with high velocity and lodges beneath the surface.
Excavator	Scoops or digs into the surface.

The two terms, penetrometer and penetrator are closely related and they can easily be confused. Penetrometry is the measurement of the mechanical properties of the subsurface by means of penetrating instruments. The measured properties include force or penetration rate. Therefore, a penetrometer is an instrument which has a sensing device to determine the resistive force. A penetrator is a device to deliver a payload, such as a penetrometer, to the subsurface. Thus, a penetrometer is a specialized penetrator.

The force required for placement of a penetrometer may be split into two components: the cone resistance, which pushes against the tip and sleeve friction which creates drag along the lateral surface. In the second workshop on *Penetrometry in the Solar System*, Kargl et al. (2008) divided penetrometers into two main categories, fast and slow. Fast penetrometers are released from a spacecraft and hit the planetary surface with enough velocity to so that their kinetic energy provides the required penetration force. Slow penetrometers are deployed from landers or rovers on the surface of the target body and penetrate the subsurface through forces applied by mechanical means. Slow penetrometers are divided into static penetrometers, which utilize a steady penetration force, and dynamic penetrometers, which apply periodic impact such as hammering.

3.2. Effects of Low Gravity Environment on Penetration

Low gravity affects the performance of penetrometers whether they are fast or slow. Fast penetrometers may not be able to obtain sufficient kinetic energy from free-fall in the gravity field to achieve the desired degree of penetration and may need propulsion specifically to increase the impact velocity. Also, a body with weak gravity would also probably lack an atmosphere that could be used to orient and direct the falling penetrometer toward the surface creating the requirement for an attitude control system.

Gravity also affects the mechanical properties of the subsurface material. A low gravity environment such as that found on asteroids and comets reduces the required penetration force because the required force is proportional to the overburden pressure and thus to gravity. Results from Deep Impact mission revealed a low-density material on comet Temple 1 (Kerr, 2005) which would ease the penetration process.

3.3. Example of Dynamic Penetrometer (PLUTO Mole)

ESA developed a small sample acquisition system and distribution tool. This instrument can be pushed only into soft and porous media with the capability to obtain subsurface samples. ESA upgraded the small sample acquisition system and distribution tool to be used for planetary investigation and called the Planetary Underground Tool (PLUTO). PLUTO (mole penetrometer) was an instrument on board of the Beagle 2 lander which was part of the Mars Express mission to Mars (Kochan, 2001). The basic design of the mole and its main components is shown in Figure 3.1. The mobile penetrometer composed of a cylinder tube which forms the housing.

A conical tip forms one of the ends of the housing and the other end is supported by a cover which has an aperture for the cables and tether which is used as a way to extract the mole from the subsurface (Gromov, 1997). The internal structure of the mole is shown in Figure 3.2.

A driving motor is placed inside the suppressor connecting the force spring to the hammering mass from one side and to the brake spring from the other side. The motor loads the force spring and compresses it. The compressed force spring delivers its energy to the hammering mass and suppressor as shown in Figure 3.3. Upon release the force spring, the hammering mass impacts the conical tip which in process push the mole into the subsurface. At the point of impact, the back spring as well as the suppressor goes along with the power spring and the hammering mass. After impact, the suppressor and the back spring start their job in absorbing unwanted reactions (Gromov, 1997).

The delivered energy by the motor to the force spring is constant; therefore, the effective energy per shock is constant which about 80 N (Stroker et al., 2003). A standard barrel is used to fix the experimental configuration with a diameter of 45 cm and height of 88 cm (Pinna et al,

2001). Figure 3.4 shows two insertion penetration tests for the PLUTO mole into quartz sand. It took the mole about 50 minutes to reach about 60 cm depth (Richter L, 2004)

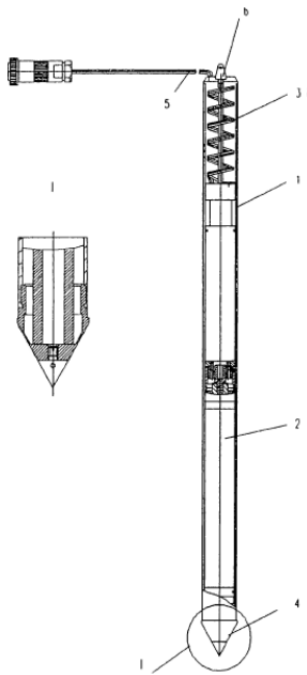


Figure 3.1. The main structure of the mole (Gromov, 1997).

- 1 – Housing
- 2 – Shock-power mechanism
- 3 – Brake spring
- 4 – Tip
- 5 – Cable
- 6 – Cover

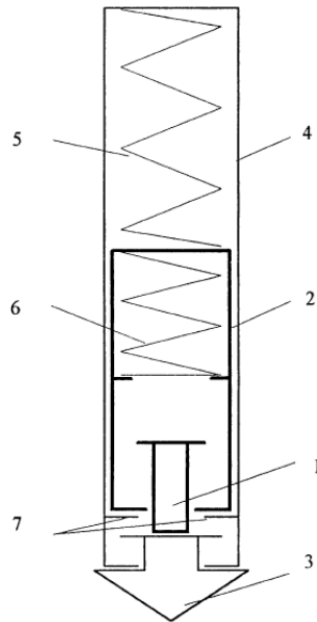


Figure 3.2. The internal structure of the mole (Gromov, 1997).

- 1- Hammer
- 2- Suppressor
- 3- Tip
- 4- Housing
- 5- Brake spring
- 6- Force spring
- 7- Lugs on the housing

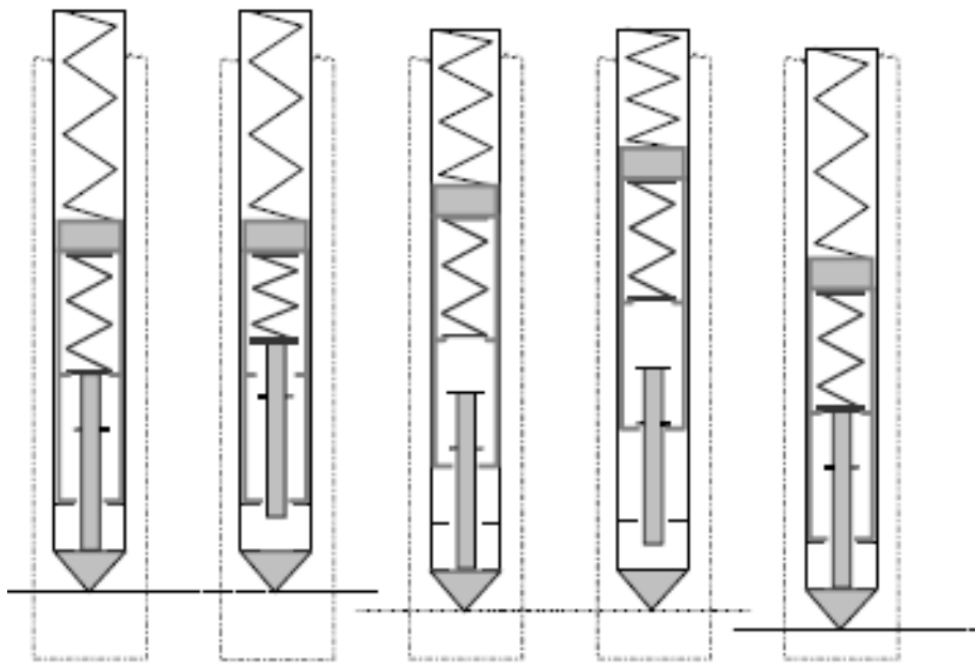


Figure 3.3.principle of mole forward hammering (Richter L, 2004)

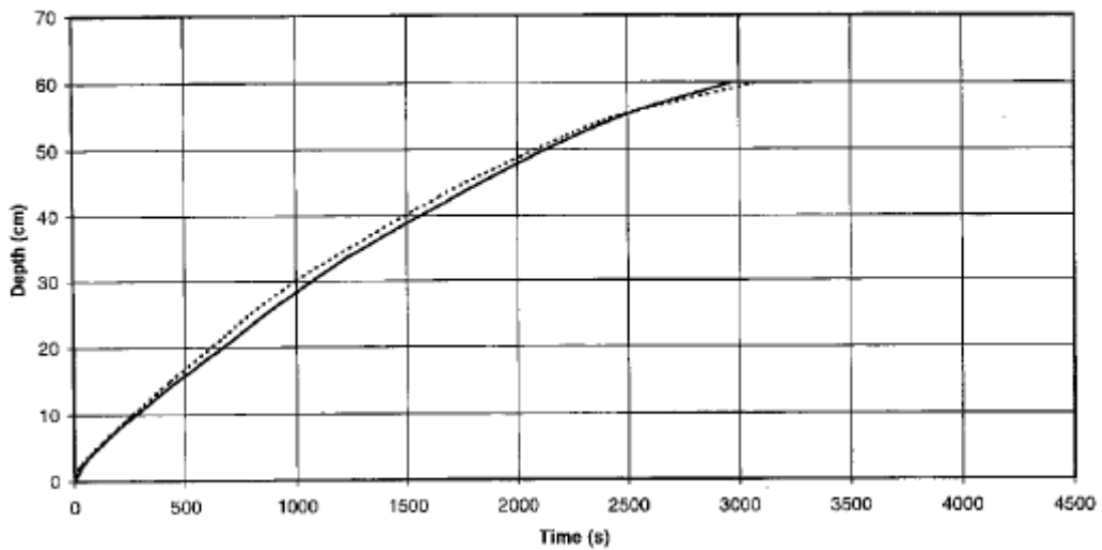


Figure 3.4.PLUTO mole insertion into quartz sand.

3.4. Penetration Testing on the Moon

Four Russian rovers called Lunokhods were sent to the Moon for surface and subsurface investigation in the period 1969 to 1977 (Leonovich et al., 1971). Two of the four rovers successfully landed on the Moon where both equipped with a cone penetrometer called PROP objected to investigate the mechanical properties of the surface and subsurface regolith (Leonovich et al., 1972). The penetrometer was cone in shape with a diameter of 5 cm and 60° apex angle (Cherkasov and Shvarev, 1973). During penetration, forces required for penetration was recorded as a function of penetration depth (Leonovich et al., 1976).

To study the effect of regolith packing on the Moon, Lunokhod 1 performed multiple penetration experiment at the same point (Fig. 3.5, Leonovich et al., 1972). Penetration resistance was observed to increase as a function of depth after the first penetration through the third one. After the first penetration, the maximum force of penetration was ~22 N corresponded to a depth of ~8 cm. After repeating the penetration at the same point, the same maximum force was achieved at ~3 cm deep for the second and third trials (Fig 3.5).

Repeated penetration at the same location caused compaction of regolith material on the Moon. However, repeating penetration can be used to estimate the subsurface density. From the character of the penetration curve of Lunokhod data, regolith material at the location where the experiments were conducted was highly uncompacted due to the force difference between curve 1 and curve 3.

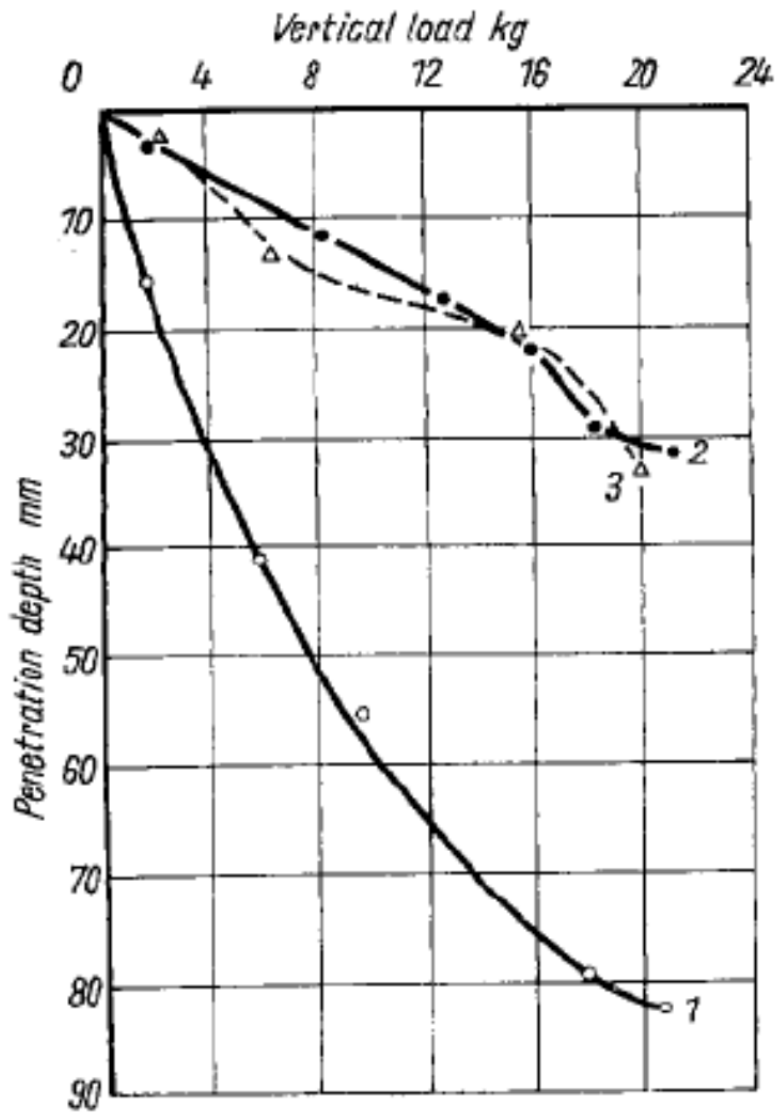


Figure 3.5. Penetration forces during investigation of lunar regolith packing capacity (Leonovich et al., 1976).

4. Experimental Apparatus

An apparatus was designed and built to measure the insertion and withdrawal forces of the probe in unconsolidated materials and to test the windows for scratching after repeated insertion/withdrawal cycles. A general illustration of the setup is shown in Figure 4.1.

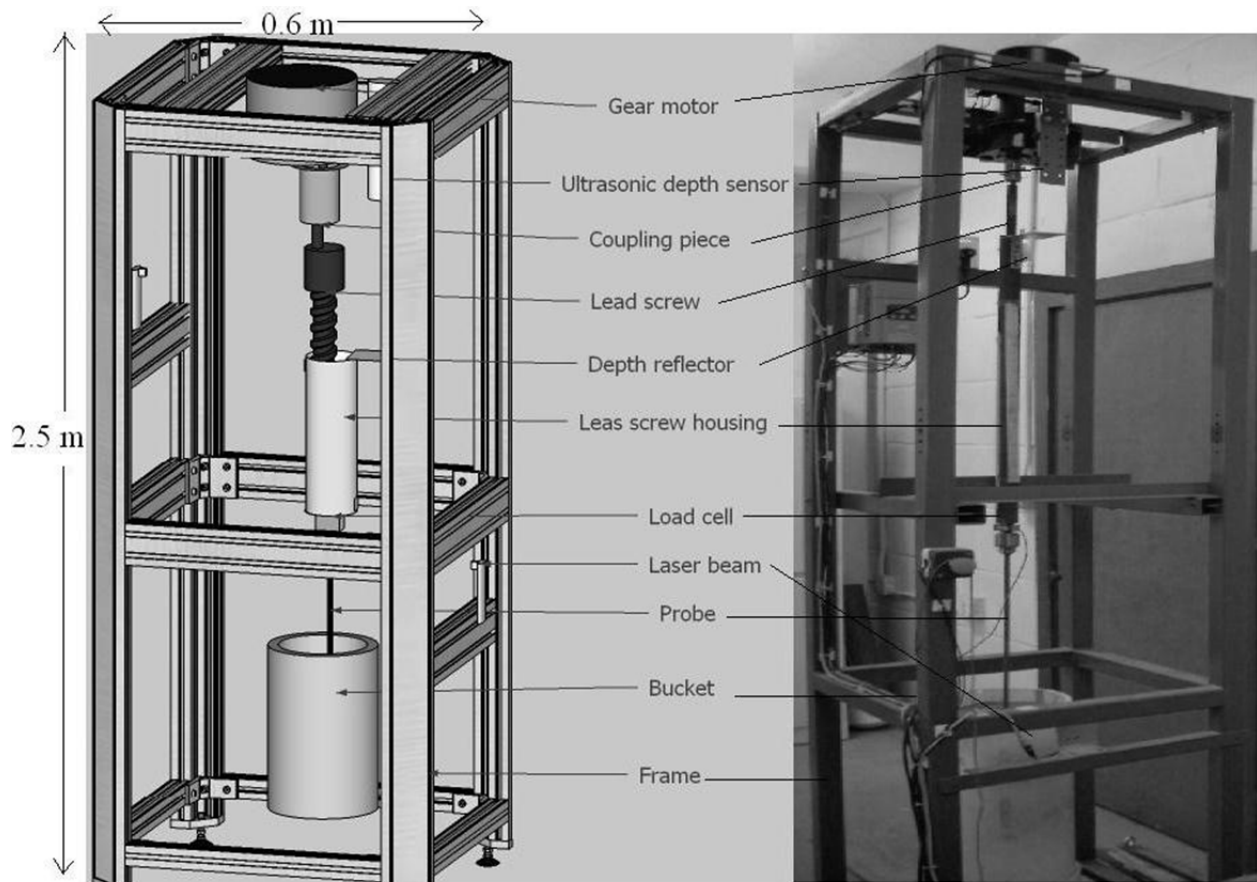


Figure 4.1. The OPRA penetration testing apparatus

A parallel shaft gear motor drives a lead screw with a major diameter of 20 mm, a minor diameter of 14.83 mm and a length of 60 cm as shown in Figure 4.2.

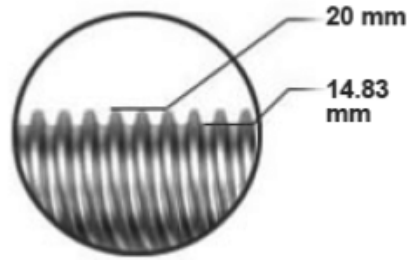


Figure 4.2. Right hand trapezoidal lead screw.

The lead screw housing is made of steel with an outside diameter of 4 cm, thickness of 5 mm and length of 80 cm. The nut outside diameter is 3.1 cm and the length is 3.8 cm as shown in Figure 4.3. The right hand bronze trapezoidal nut is attached at the top of the housing as seen in Figure 4.4.

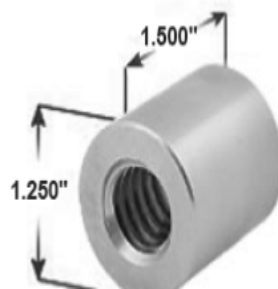


Figure 4.3. Right hand trapezoidal nut.

The role of the housing is to move up and down in correspondence to the forward and backward movement of the motor. The housing has two reflective laser sensors, one at the top of the housing and the other one is at the bottom as shown in Figure 4.4. It is their role to stop the automated program if one of the lasers hits the reflective plates.

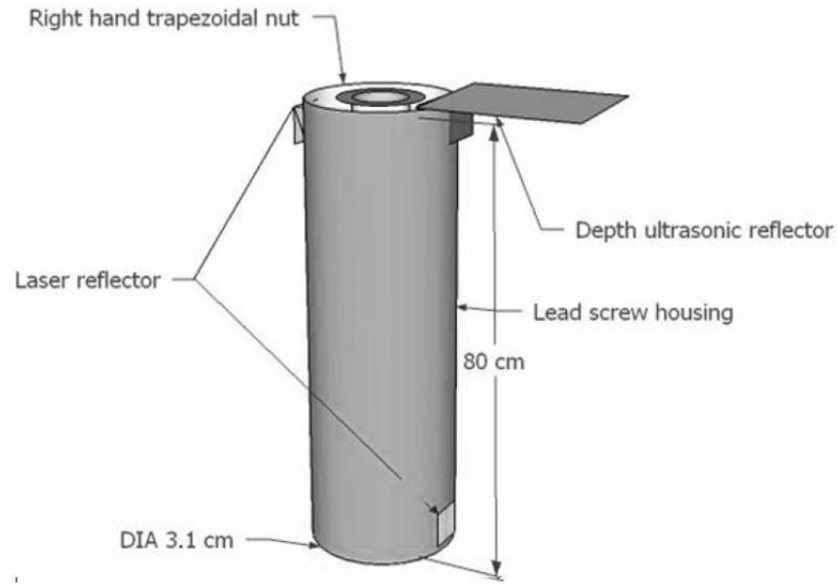


Figure 4.4. The lead screw housing with the laser reflectors, trapezoidal nut and depth reflector.

The motor speed is run at 18 rpm with an input power of 1/3 horse HP and is capable of working in a reversible mode. It is equipped with a built-in fan for cooling. The gear motor shaft has a diameter of 1.9 cm and length of 3.81 cm (Figure 4.5).



Figure 4.5. Parallel shaft gear motor

The coupling between the motor and the lead screw is realized by using a two-way metal sleeve connector. At the top part of the coupler, the motor shaft is pushed in while at the bottom part, the lead screw is attached. The coupling piece is secured to the motor shaft by tying two

screws in the gap with in the shaft. A hole is drilled in the lead screw for attaching it to the coupling piece by means of a screw. This screw plays an important role where it transfers the torque from the motor to the lead screw. The coupling piece provides high holding capacity between the motor shaft and the lead screw as seen in Figure 4.6.

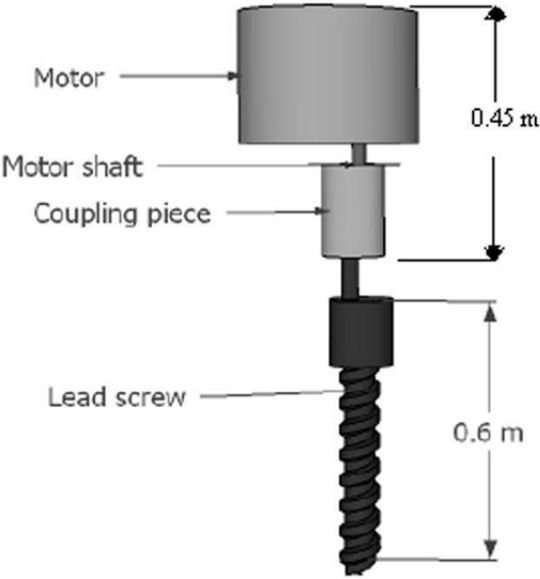


Figure 4.6.coupling piece connecting the gear motor to the leas screw.

An MLP-1K load cell is is attached at the bottom of the housing by means of 3/8-24 inch thread. The dimension of the load cell is shown in Figure 4.7 and Table 4.1. The complete specification of the load cell is shown in Table 4.2.

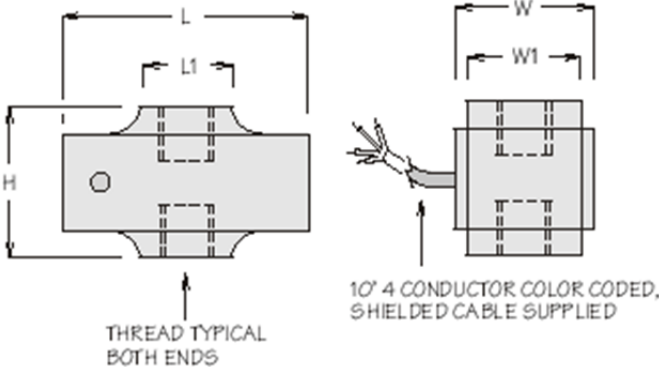


Figure 4.7. Load cell dimensions

Table 4.1. Load cell dimensions in inches

Model	Capacity LBS	L	L1	W	W1	H	Thread	Thread depth	Wt. Ozs
MLP-1K	1000	1.8	0.6	0.93	0.75	1	3/8-24	0.375	3

Table 4.2. MLP-1K specifications

Rated Output (R.O.): 2 mV/V nominal	2 mV/V nominal
Nonlinearity	0.1% of R.O.
Hysteresis	0.1% of R.O.
Nonrepeatability	0.05% of R.O.
Zero Balance	1.0% of R.O.
Compensated Temp. Range	60° to 160°F
Safe Temp. Range	-65° to 200°F
Temp. Effect on Output	0.005% of Load/°F
Temp. Effect on Zero	0.005% of R.O./°F
Excitation Voltage	10 VDC
Safe Overload	150% of R.O.

A DPM-3 output panel was used as the load cell meter. It is attached to the load cell and it is calibrated to give output reading in lbs with an accuracy of 0.01%. Figure 4.8 shows the DPM-3 while Figure 4.9 shows the colour code wiring with the load cell.



Figure 4.8. Digital Panel Mount (DPM-3)

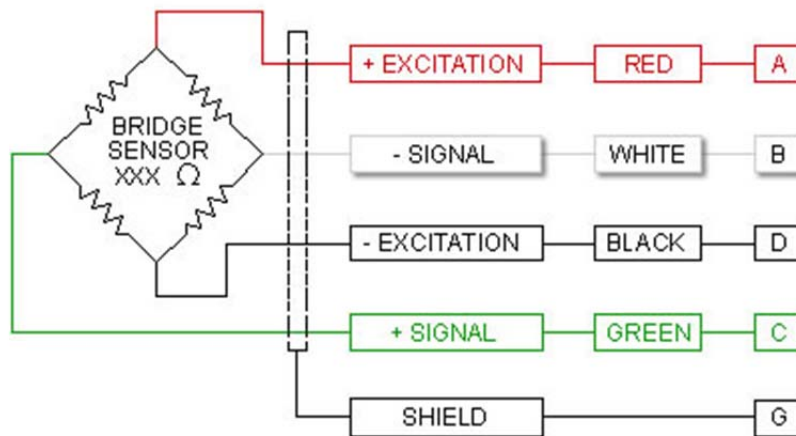


Figure 4.9. Meter, load cell colour code

An ultrasonic distance sensor is placed on the top of the penetration stand. By measuring the distance from this sensor, which rides along with the sleeve, and the top of the regolith the penetration distance of the probe into the regolith can be calculated continuously. It has a beam angle of 8 degrees and a maximum range of 150 cm. The sensor and its dimensions are shown in Figure 4.10. At the top of the housing, a reflective aluminium surface is mounted in order to reflect the ultrasonic waves which generates by the sensor and from where the depth sensor give depth measurements.

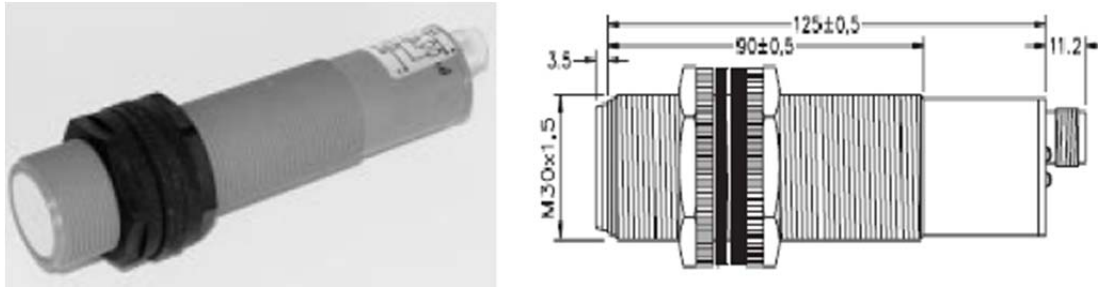


Figure 4.10. Ultrasonic sensor and its dimensions in mm.

An automated control system was designed by SPAC grad student Obadiah Kegege and Lauren Foster, a summer 2008 REU student. A programmable logic controller (PLC) was used and was programmed using one of the ladder logic programs. IC200UAL006 in the candidate microcontroller and proficy HMI/SCADA-CIMPLICITY is the ladder logic program. The ladder logic program has a Human Machine Interface (HMI) feature where the whole penetration test is monitored and controlled through personal computer (PC).

The Graphical Human Interface (GHI) of the data collecting software is composed of one main screen with three other screens embedded inside it. The main panel has buttons which can be divided into two main groups: controlling the penetration testing and indicating the status of the experiment. During penetration two parameters were being monitored: the penetration force and penetration depth. Both of these parameters were recorded simultaneously through the automated system.

The calibration screen is used to set the motor speed, penetration depth and the penetration force, as shown in Figure 4.11.

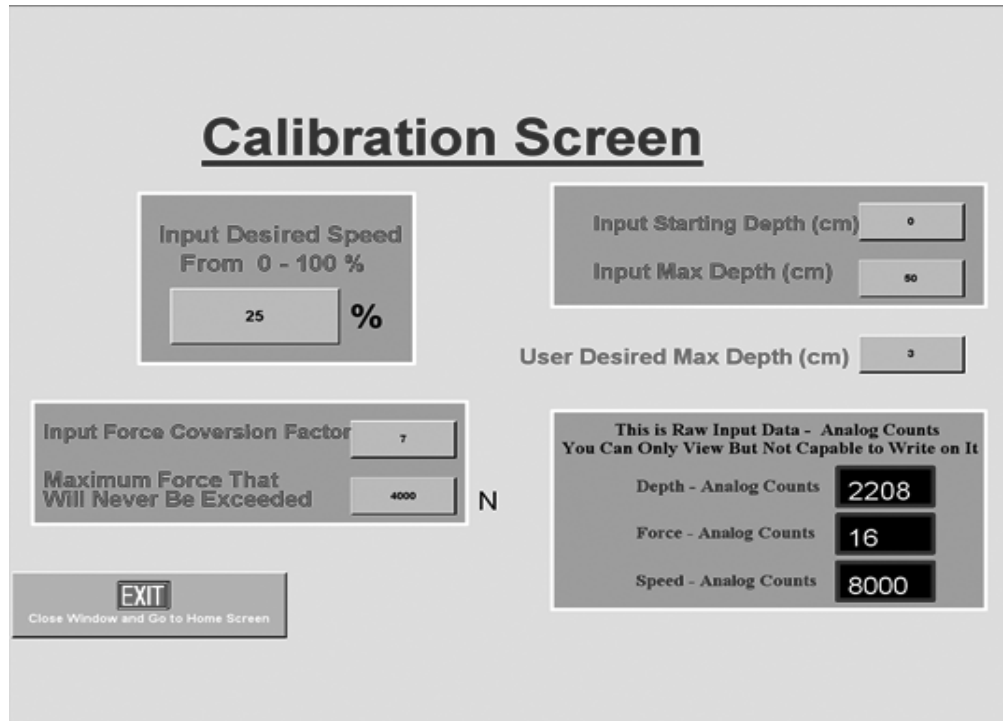


Figure 4.11. Calibration screen

The motor speed controls are expressed in a scale from 0 % to 100 % where 0% corresponds to 0 rpm of the motor and 100 % is the maximum motor speed. We calibrated these percentages to actual penetration speeds as follows:

16 % → 1 mm/sec,

25 % → 2 mm/sec,

38 % → 3 mm/sec and

60 % → 4 mm/sec

The user can set the starting, working, and maximum depth in cm. The maximum depth is the most the apparatus will allow and usually corresponds to the probe's length. For example, if the user wants a probe which is 50 cm in length to be penetrated to about 5 cm from the surface for 200 times continuously. Then, the input starting depth is set to zero, the input maximum depth is set to 50 (probe length) and the user desired maximum depth is 5 cm. the probe will start from zero until 5 cm depth is reached then the probe will move upward till zero and start again until the 200 times are over.

Three outputs shown in the main screen, the motor speed which in mm/sec, the penetration depth in cm and the corresponding penetration force which in Newton's as seen in Figure 4.12.

The Insert/Remove buttons activate the probe to be pushed downward and to be pushed upward. The user has the authority to stop any of these buttons whenever the user prefers. The insert probe condition is deactivated when the probe reaches a desired depth configured by the user and a text message will blink showing that the probe reached its maximum depth. The remove probe button stops its functionality when the probe is removed from certain depth and a text message will blink showing that the probe is fully removed.

An important feature in the HMI main panel which it's capability of coordinating of subsurface imaging by setting the exposure time from Input IR Exposure Time button. When the probe at this stage a text message will blink shows that the probe is acquiring data and when the exposure time ends another text message will blink shows that the data acquisition is complete.

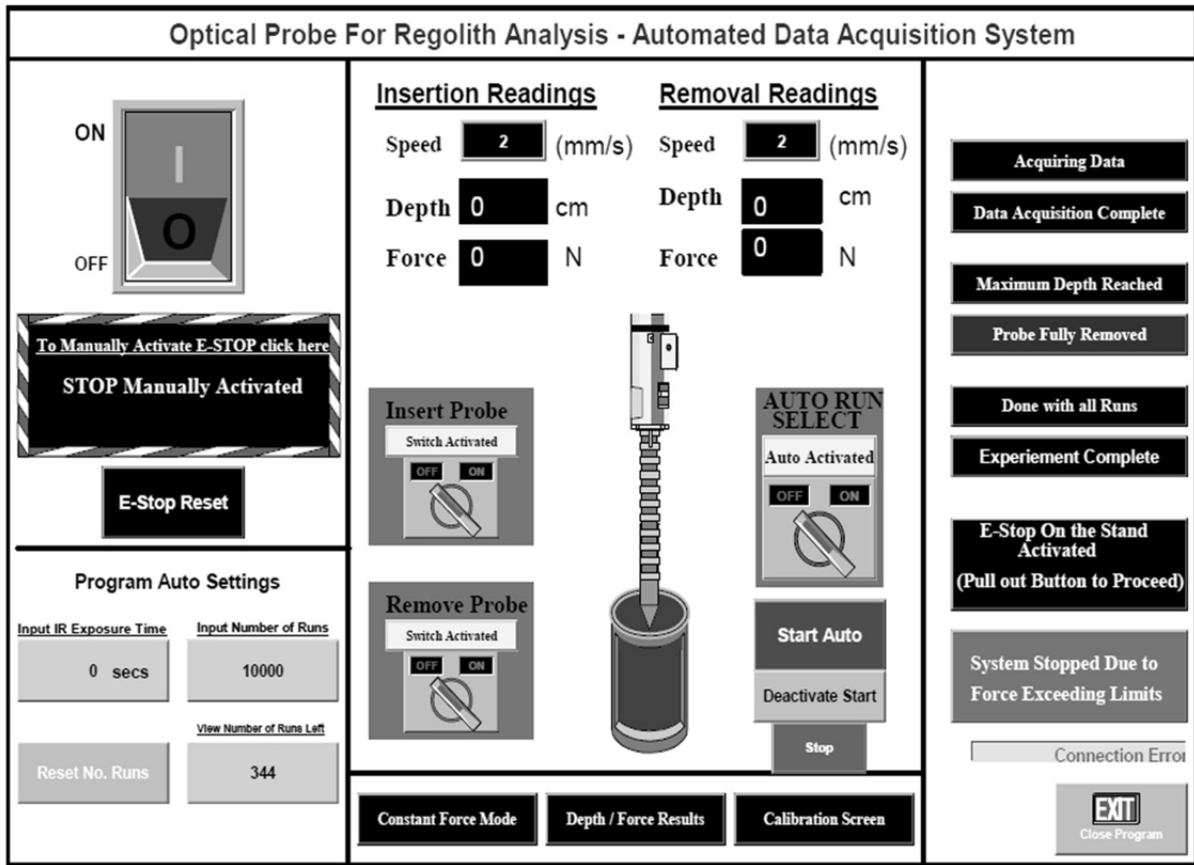


Figure 4.12. Graphical User Interface (GUI) screen.

In order to use the Auto Run Select button, two steps should be carried out. First, the user has to set the number of runs by introducing the number into the Set the Number of Runs button which is located under Program Auto Select. View the number of runs button decreases as the Auto Run start to function and it shows the rest number of runs which are needed to complete the experiment.

The number of runs can be changed by using the Reset Number of Runs button. When the experiment is over, the Auto Run Select button needs to be deactivated and stop the program by pressing on Stop button.

The depth versus force screen shows the output results of the penetration testing experiment in an x-y plane as shown in Figure 4.13. The x-axis is configured by the penetration depth which in (cm) and the y-axis has the penetration force (N). This chart can be printed directly from the screen or the data could be saved in another format such as Excel data sheet.

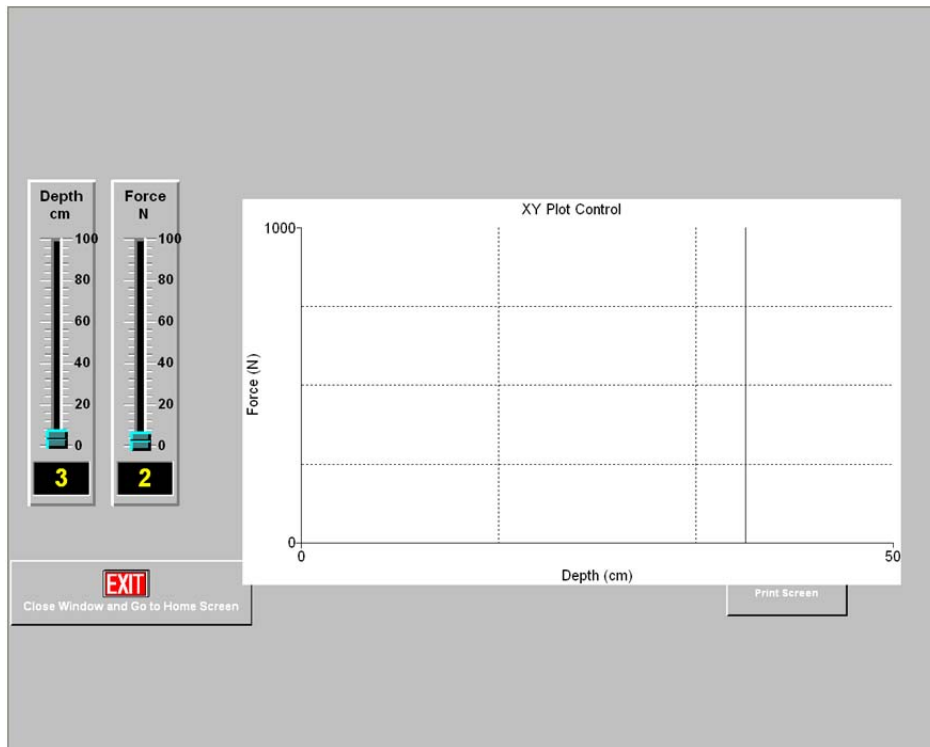


Figure 4.13. Depth versus force screen

The constant force mode screen is used when the user wants to run penetration testing under constant force instead of constant speed. The input desired force button is set to the user desired force as shown in Figure 4.14. In this mode the output results will have the form of penetration time versus penetration depth.

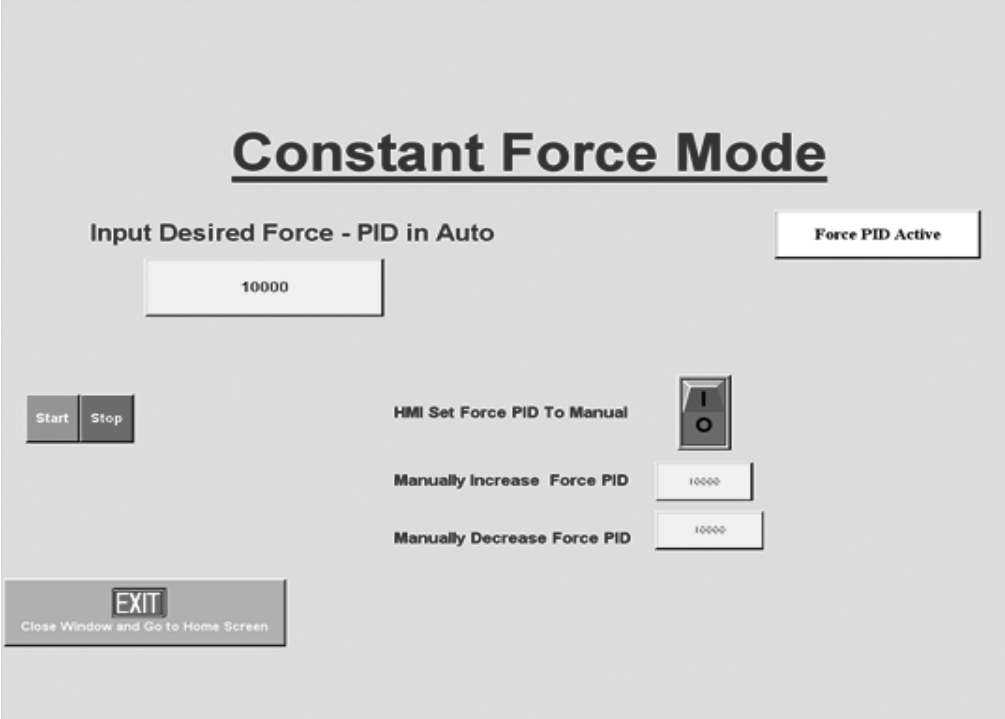


Figure 4.14. Constant force screen

5. Experimental Procedure

5.1. Validation of the Force Sensor

A comparison was made between the compression forces from the load cell and from a mechanical balance in order to validate the force sensor. The procedure was as follows:

- 1) A probe attached to the load cell.
- 2) By turning the motor on, the probe is pushed down against a balance which has a capacity of 200 kg force. The balance is on the floor, not on regolith, and is immobile in the vertical direction.
- 3) An output value in kilograms is shown on the balance and a corresponding output value from the load cell appears on the transducer.
- 4) Two reading appear in Figure 5.1 and shows good agreement. A conversion factor was chosen in order to calibrate the force out of the HMI close to the balance results.

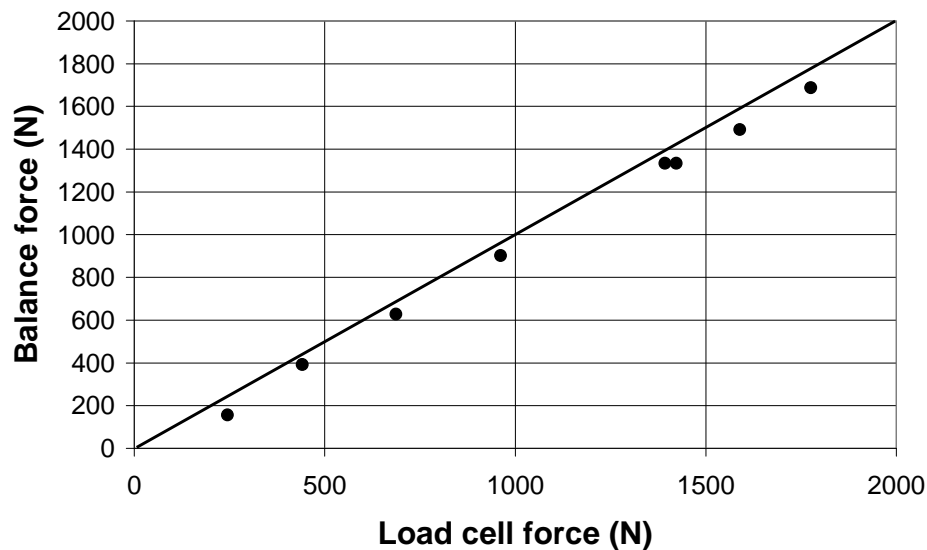


Figure 5.1. Validation of the load cell readings in N with the balance reading in N.

5.2. Loading the Regolith Sample

Samples were filled in a container which has a diameter of 25 cm and it is 65 cm long. The material was poured in by layers, each with a mass of 5 kg, and the container was shaken in order to differentiate the regolith and to be sure that it was compacted. The corresponding height was measured after each layer addition and compaction.

5.3. Penetration Probes

A list of twenty spikes categorized into six groups as shown in Table 5.1 were used during the project. These spikes vary in diameter, shape, length and tip apex angle to envelop most of the variables throughout the experimental plan. Penetration testing took place at a constant speed of 2 mm/sec.

Table 5.1. List of twenty spikes used in the penetration testing

Series 1	Diameter (cm)	Length (cm)	Tip Length (cm)	Tip Angle (Deg)
Spike 1	0.5	50	0	180

Series 2	Diameter (cm)	Length (cm)	Tip Length (cm)	Tip Angle (Deg)
Spike 1	0.9	50.8	1.8	30
Spike 2	0.9	50.8	0.9	60
Spike 3	0.9	50.8	0.6	90
Spike 4	0.9	50.8	0.3	120

Series 3	Diameter (cm)	Length (cm)	Tip Length (cm)	Tip Angle (Deg)
Spike 1	1.2	51	2.4	30
Spike 2	1.2	51	1.2	60
Spike 3	1.2	51	0.7	90
Spike 4	1.2	51	0.4	120

Series 4	Diameter (cm)	Length (cm)	Tip Length (cm)	Tip Angle (Deg)
Spike 1	1.9	50.8	3.4	30
Spike 2	1.9	50.8	1.7	60
Spike 3	1.9	50.8	1	90
Spike 4	1.9	50.8	0.6	120

Series 5	Diameter (cm)	Length (cm)	Tip Length (cm)	Tip Angle (Deg)
Spike 1	2.5	51	4.6	30
Spike 2	2.5	51	2.2	60
Spike 3	2.5	51	1.35	90
Spike 4	2.5	51	0.8	120

Series 6	Perimeter (cm)	Length (cm)	Tip Length (cm)	Tip Angle (Deg)
Spike 1	4	58	2.	30
Spike 2	4	58	0.8	60
Spike 3	4	58	0.5	90

5.4. Procedure for Conducting the Penetration Experiments

By turning on the insert button from the GHI in Figure 4.12, the motor drove the lead screw and the housing to push the probe down the subsurface with a constant speed of 2 mm/sec to a depth of 50 mm. The weight of probe was not considered during the penetration experiment because the transducer readout was zeroed before each penetration test with the probe in place hanging in air. During the insertion process, a real time resistance force was recorded as a function of depth. By pressing the remove button in Figure 4.12, the probe is removed from the subsurface with the same insertion speed.

5.5. Regolith Particles Size Distribution

The distribution of the particle sizes for the three regolith materials was obtained by sieving. Figure 5.2, 5.3 and 5.4 show the resulting particle size distribution curves for JSC Mars-1, JSC Mars -2 and Mojave soil. The tested JSC Mars-1 has 16% medium size particles (>0.5 mm) and 84% fine particles (< 0.3 mm), JSC Mars-2 has 1.5% medium size particles and 98.5% fine particles and Mojave soil has about 100% fine particles (Peters et al., 2008).

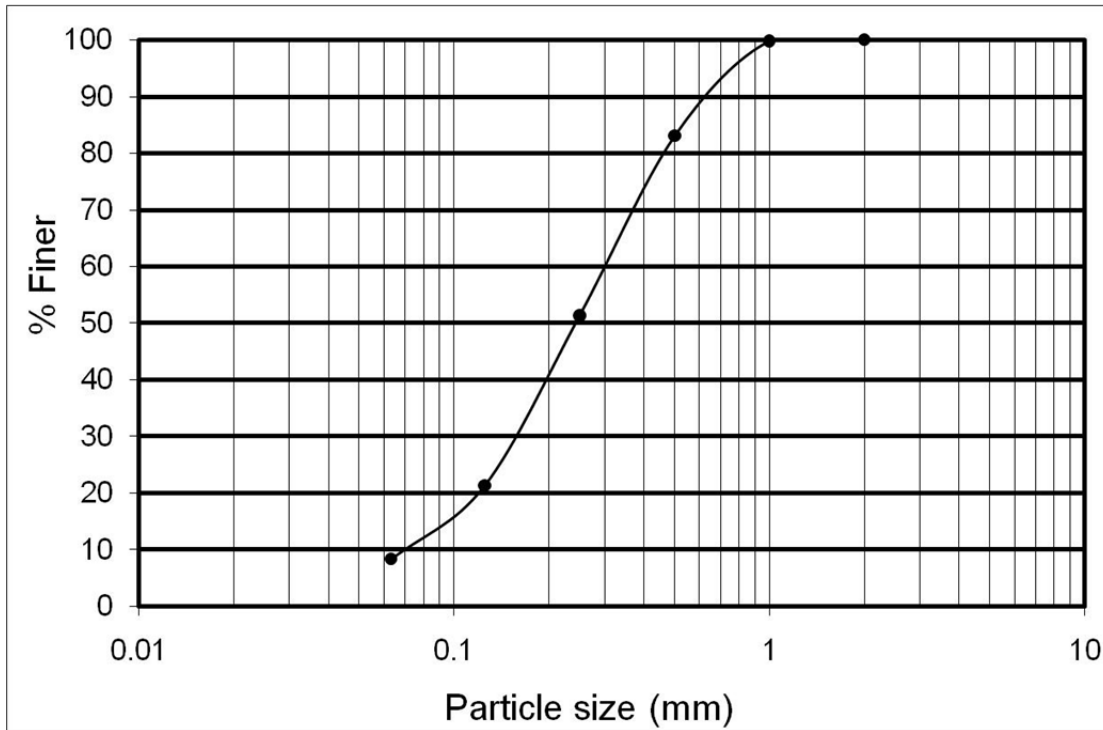


Figure 5.2. Particle size distribution for JSC Mars-1.

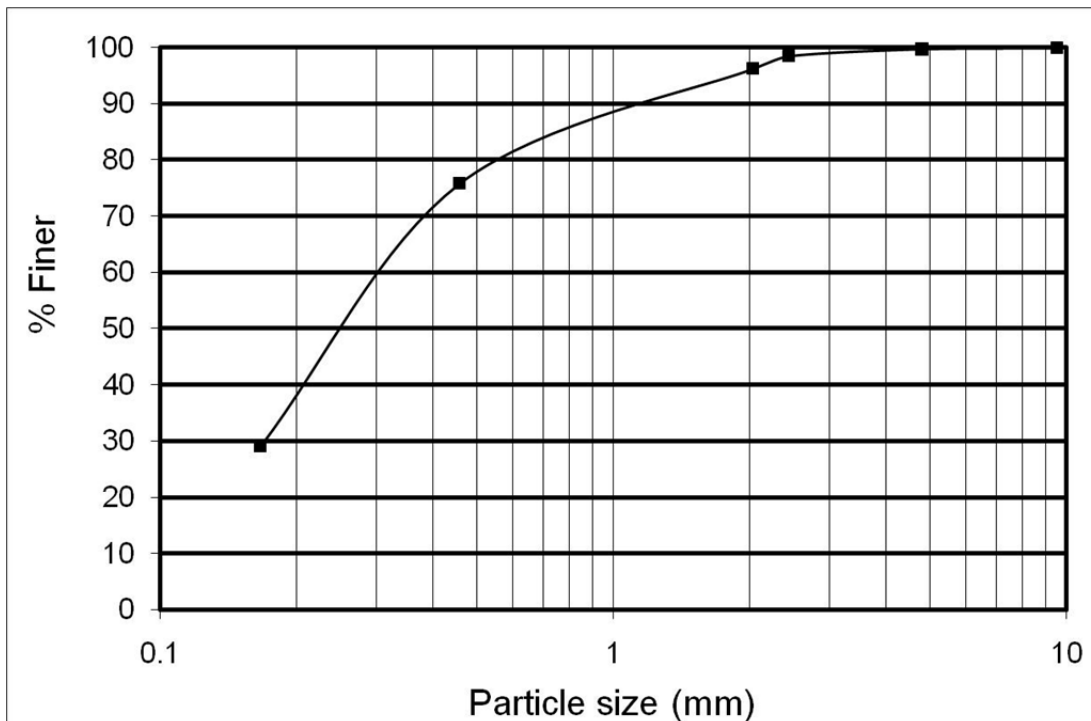


Figure 5.3. Particle size distribution for JSC Mars-2.

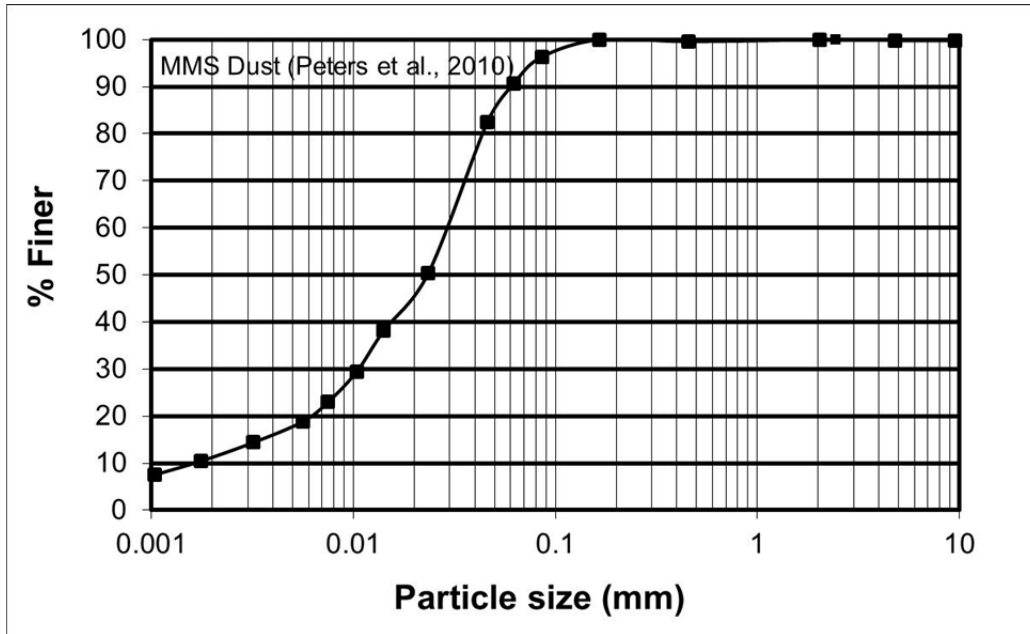


Figure 5.4. Particle size distribution for Mojave soil.

6. Experimental Results

6.1. Effect of Bulk Density

Bulk density has a significant effect on the penetration force. In order to simulate a worse-case scenario, we compacted the regolith materials as fully as possible before most experiments. Figure 6.1 and 6.2 shows the variation of bulk density of JSC Mars-1 and JSC Mars-2 as a function of depth.

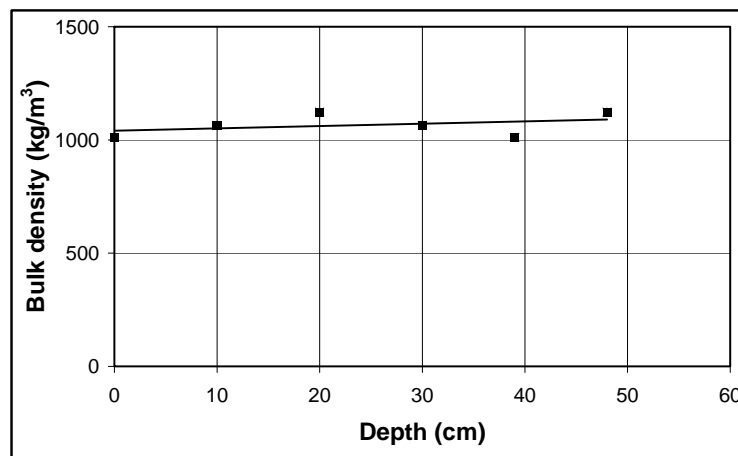


Figure 6.1. Variation of bulk density with depth in JSC Mars-1.

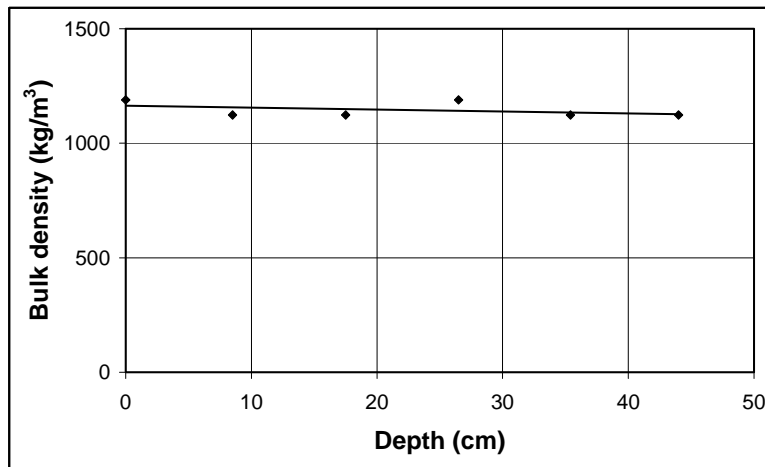


Figure 6.2. Variation of bulk density with depth in JSC Mars-2.

6.2. Effect of Compaction

It was found that in JSC Mars-1, and presumably in other regolith materials, the insertion force required was a strong function of the bulk density. A cylindrical container ($D = 25.1$ cm, $H = 45$ cm) was filled with JSC Mars-1 with a bulk density of 895 kg/m^3 and three insertion and removals were conducted at this bulk density. The container was shaken by hand in order to compact the material to a higher bulk density, followed by three more penetration measurements. This procedure was repeated to give the results in Figure 6.3.

The degree of compaction was found to have a profound impact on the forces required for probe penetration. At a bulk density of 895 kg/m^3 , the 0.9 cm diameter probe required only about 20 N to penetrate to a depth of 40 cm while it took about twenty times more force to reach the same depth when the bulk density was 1061 kg/m^3 . The three insertions and withdrawals of the probes themselves did not seem to compact the material to a measurable degree.

The same effect observed in Mojave soil. At 40 cm deep, the force of penetration increased from about 50 N to 700 N when the regolith bulk density increased from density from 1180 to 1440 kg/m^3 (Figure 6.4). For the rest of penetration tests, we performed all subsequent experiments at the maximum compaction density to bring consistency into our results and to find the maximum penetration forces that might be needed.

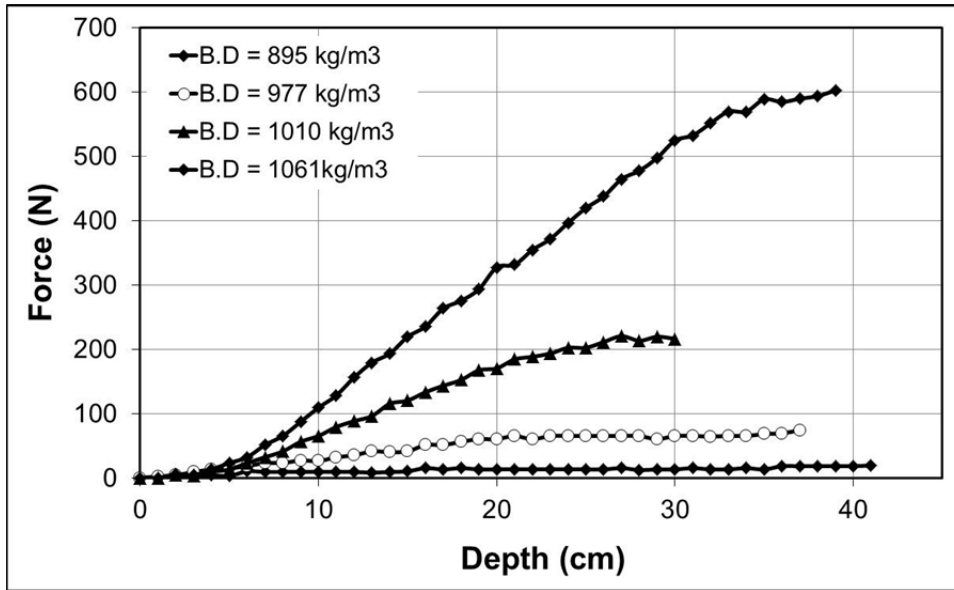


Figure 6.3. Penetration force as a function of depth in JSC Mars-1 under different bulk densities (D = 0.9 cm, T.A = 60°).

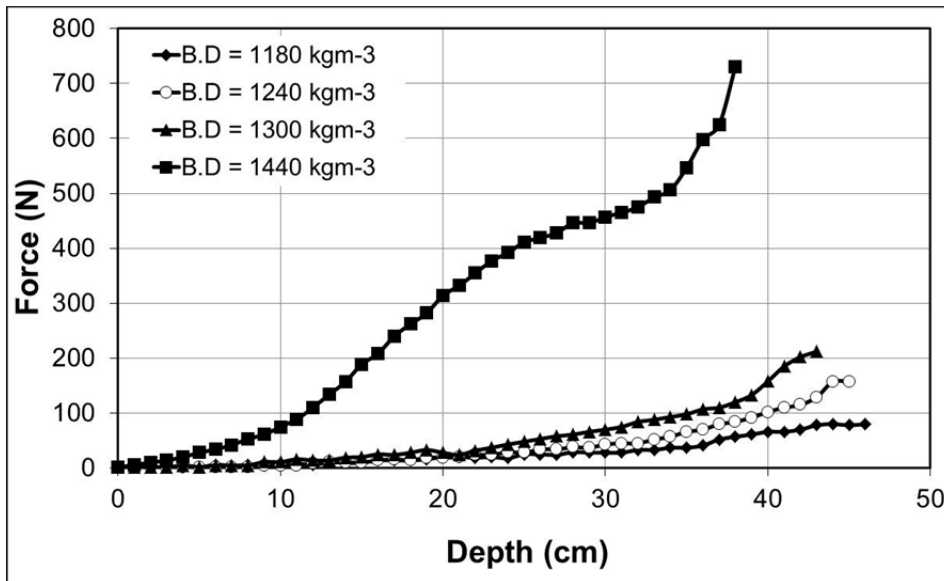


Figure 6.4. Penetration force as a function of depth in Mojave soil under different bulk densities (D = 0.9 cm, T.A = 60°).

6.3 Effect of Penetration Speed

Four different vertical penetration speeds were tested (Figure 6.5): 1, 2, 3 and 4 mm/sec into sand with a bulk density of 1700 kg/m^3 using the same 0.9 cm spike with a tip angle of 60° . There was no significant difference in the required forces. For the rest of the project we decided to use 2 mm/sec since the actual penetration rate from a planetary lander or rover will probably be on the slow side.

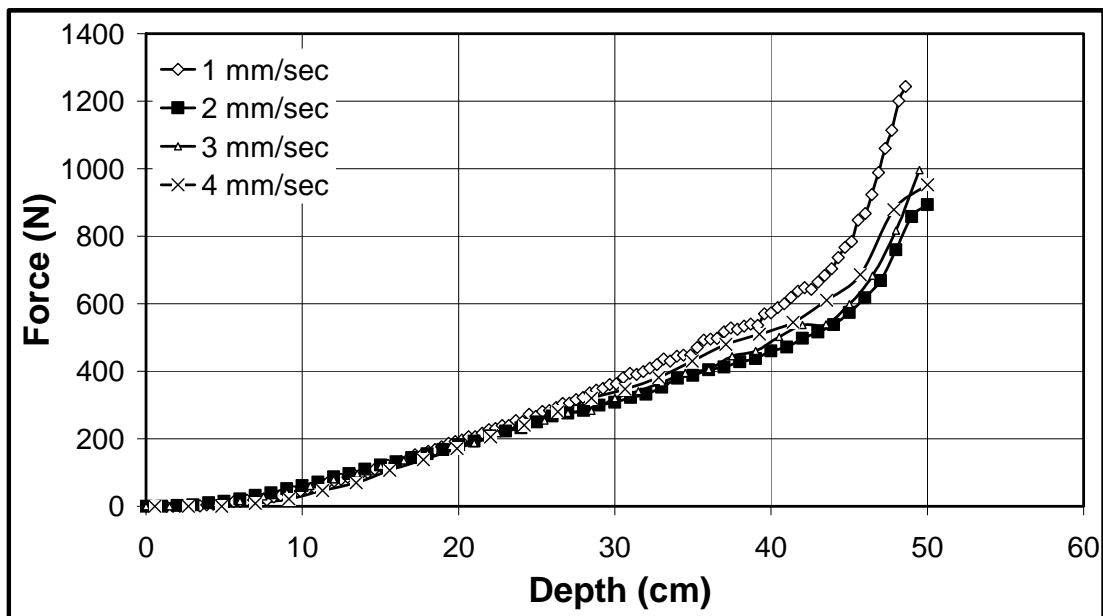


Figure 6.5. Penetration force as a function of depth in sand for different speeds.

($D = 0.9 \text{ cm}$, $T.A = 60^\circ$)

6.4 Effect of Tip Angle

Each probe was made with four tip angles: 30, 60, 90 and 120°. It was expected that the tip angle would influence the penetration force to reach a given depth, but the required forces were insensitive to tip angle.

JSC Mars-1

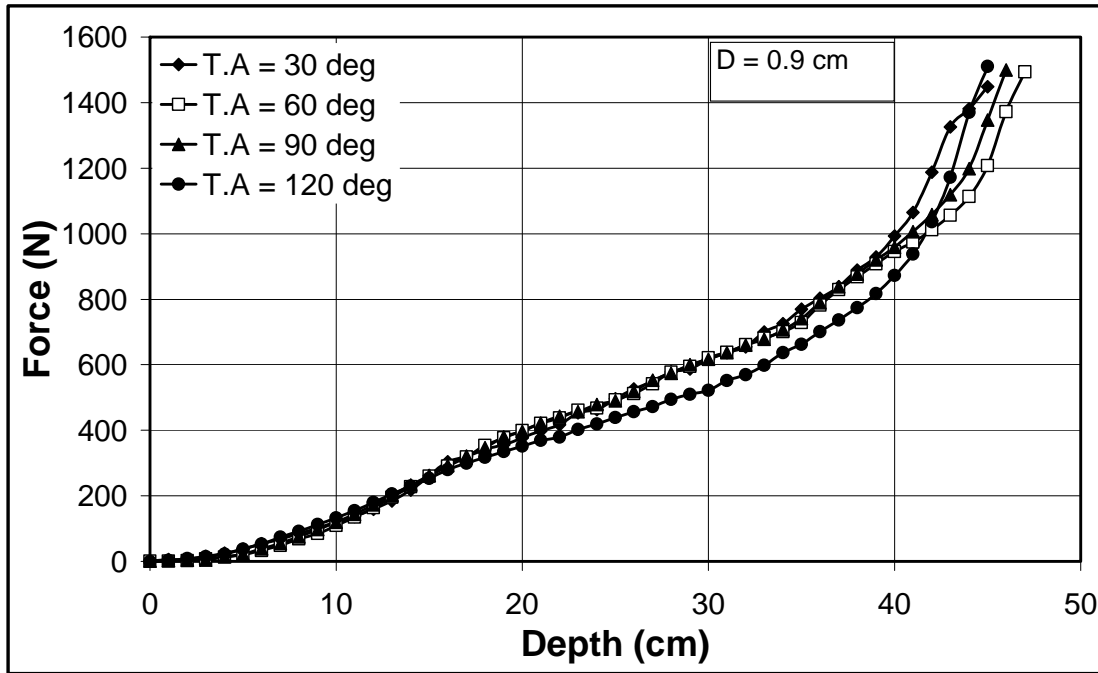


Figure 6.6. Penetration force as a function of depth in JSC Mars-1 for different tip angles and the same probe diameter ($D = 0.9 \text{ cm}$).

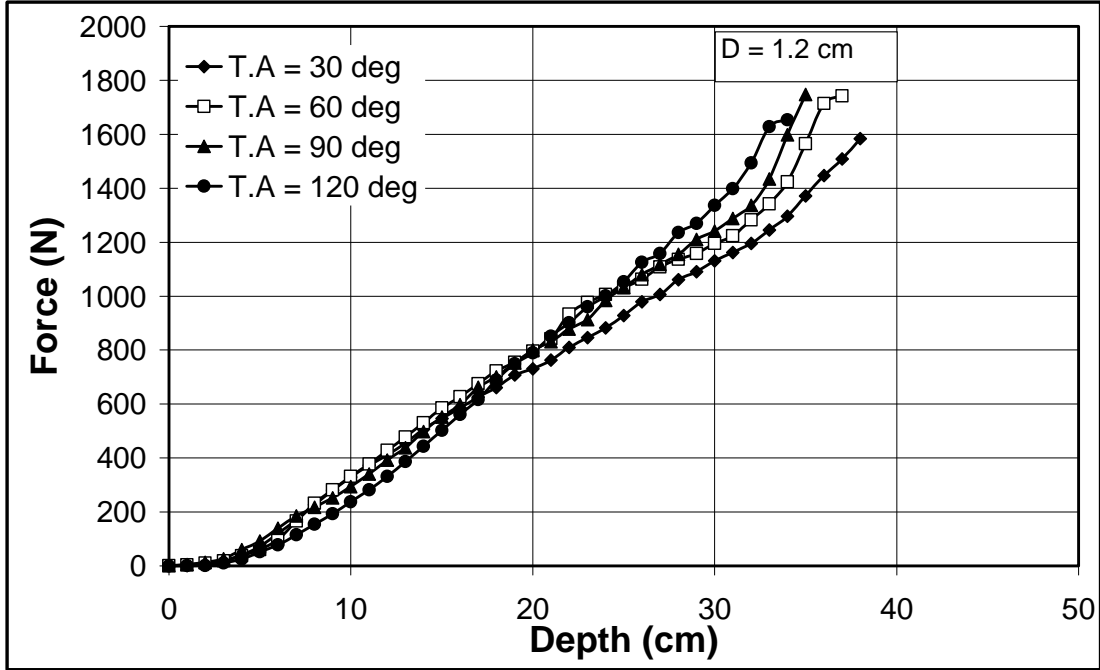


Figure 6.7. Penetration force as a function of depth in JSC Mars-1 for different tip angles and the same probe diameter ($D = 1.2$ cm).

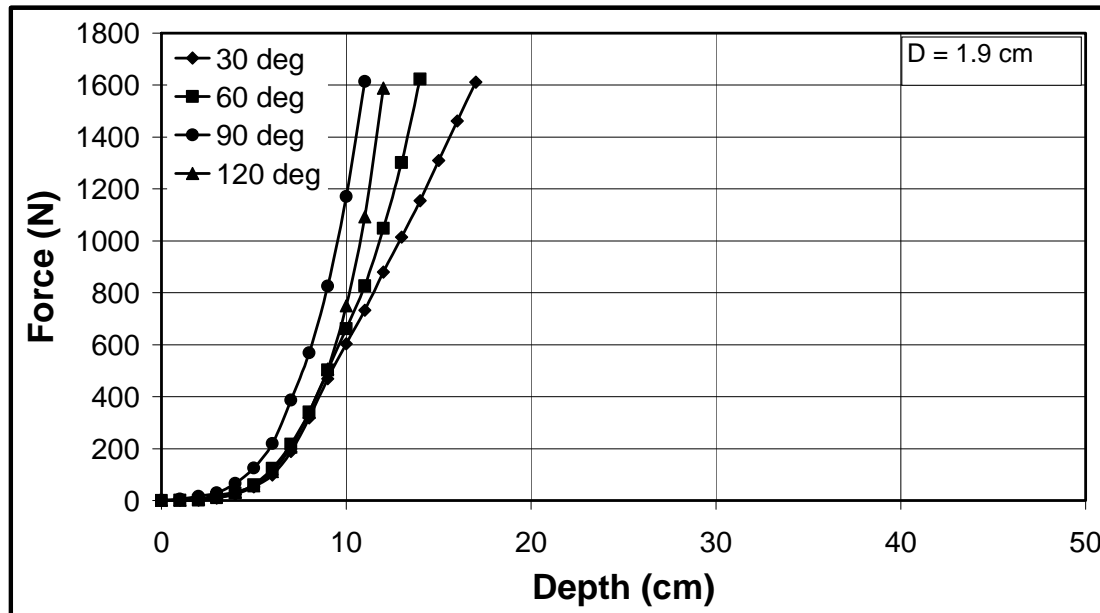


Figure 6.8. Penetration force as a function of depth in JSC Mars-1 for different tip angles and the same probe diameter ($D = 1.9$ cm).

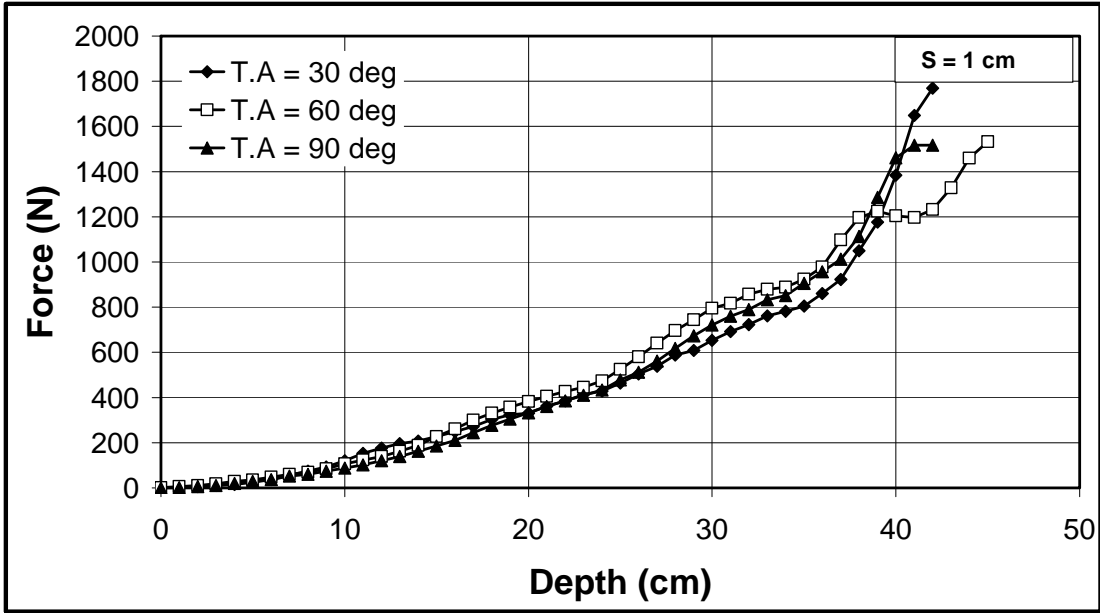


Figure 6.9. Penetration force as a function of depth in JSC Mars-1 for different tip angles and the same square probe ($S = 1$ cm).

JSC Mars-2

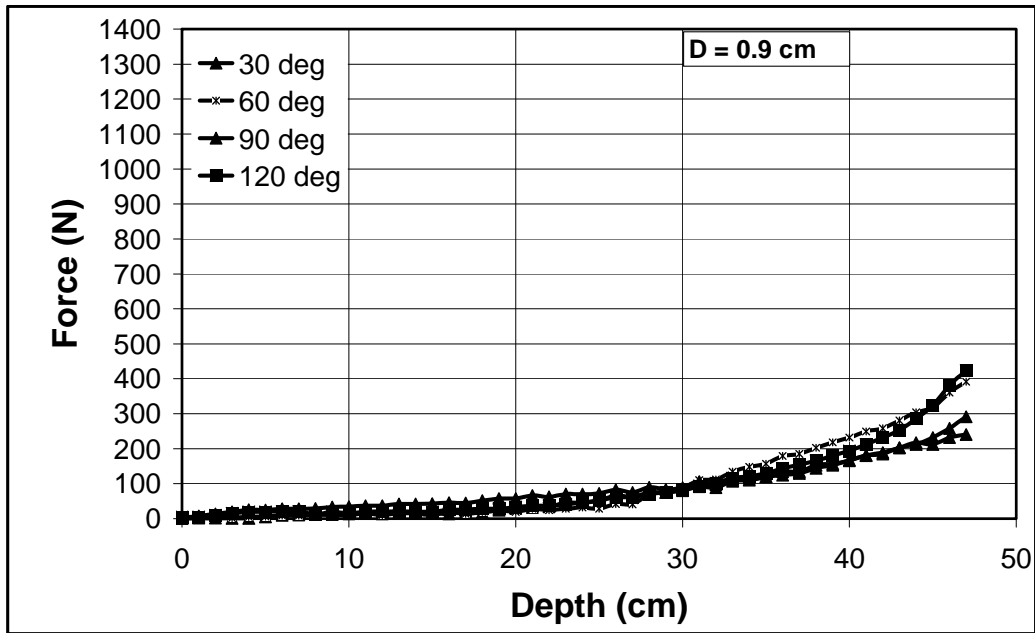


Figure 6.10. Penetration force as a function of depth in JSC Mars-2 for different tip angles and the same probe diameter ($D = 0.9$ cm).

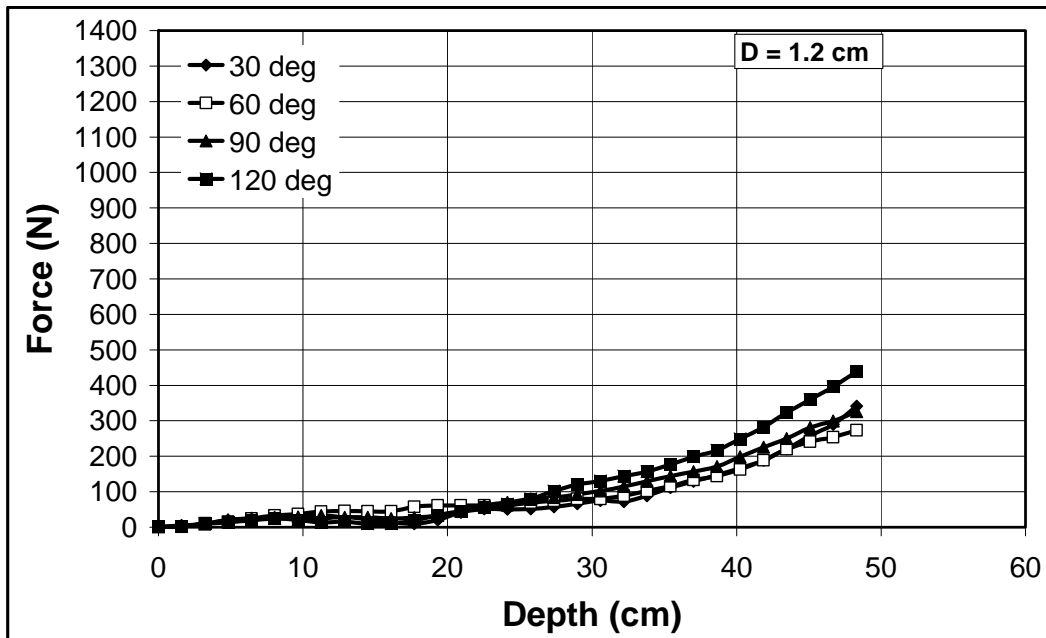


Figure 6.11. Penetration force as a function of depth in JSC Mars-2 for different tip angles and the same probe diameter ($D = 1.2$ cm).

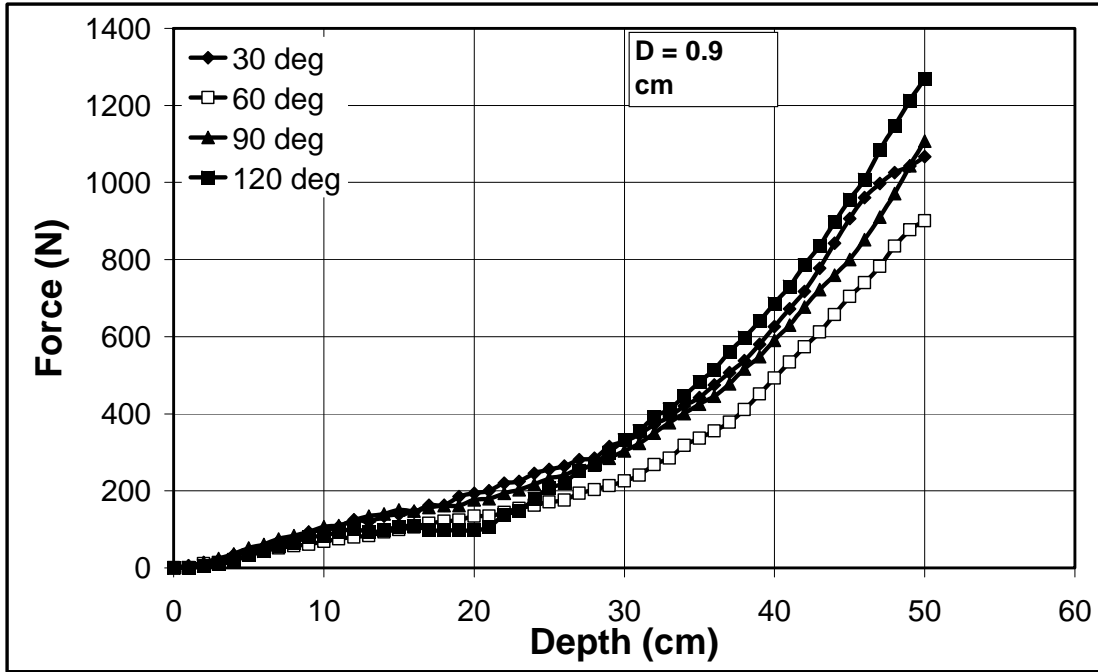


Figure 6.12. Penetration force as a function of depth in JSC Mars-2 for different tip angles and the same probe diameter ($D = 1.9$ cm).

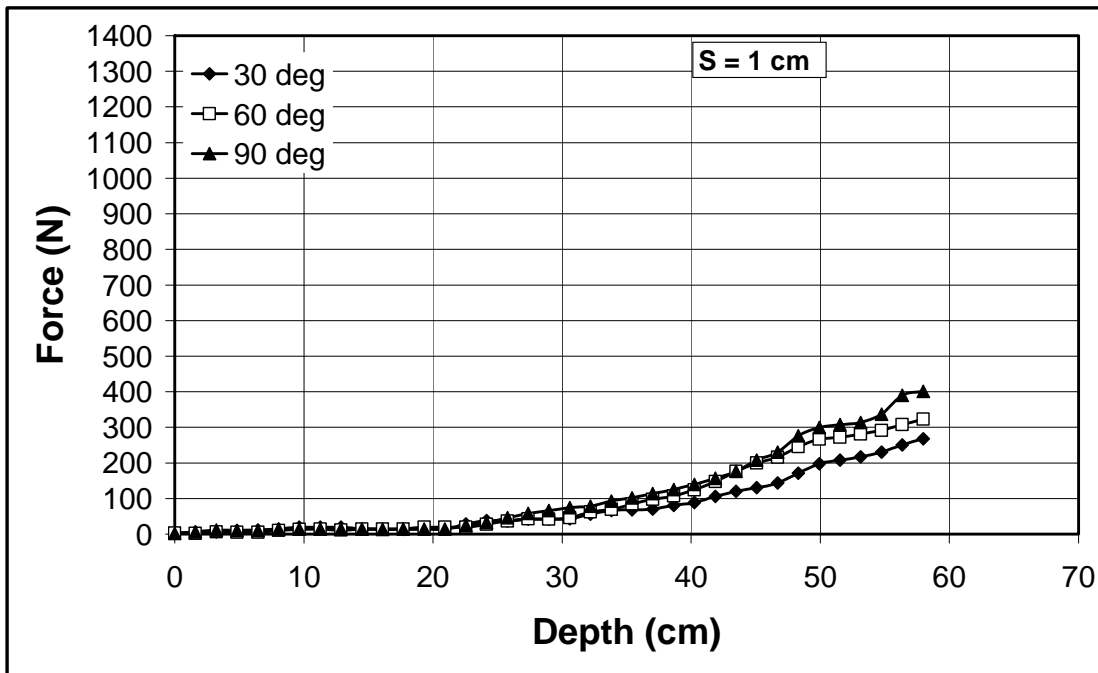


Figure 6.13. Penetration force as a function of depth in JSC Mars-2 for different tip angles and the same square probe ($S = 1$ cm).

6.4. Effect of Cross Section Shape

Probes with different cross-section shapes (circular and square) and tip angles (30, 60 and 90°) were tested in sand, JSC Mars-1 and JSC Mars-2 in order to investigate how the probe's shape affects the insertion and removal force of penetration as a function of depth. The circular probe had a diameter of 1.20 cm and the square probe had a side length of 1.00 cm. This gave perimeters of 3.77 and 4.00 cm, respectively, and cross-section areas of 1.13 and 1.00 cm. Since the square probe had a larger perimeter and the circular probe had a larger area, we hoped that we could identify which factor dominated the insertion force.

Sand

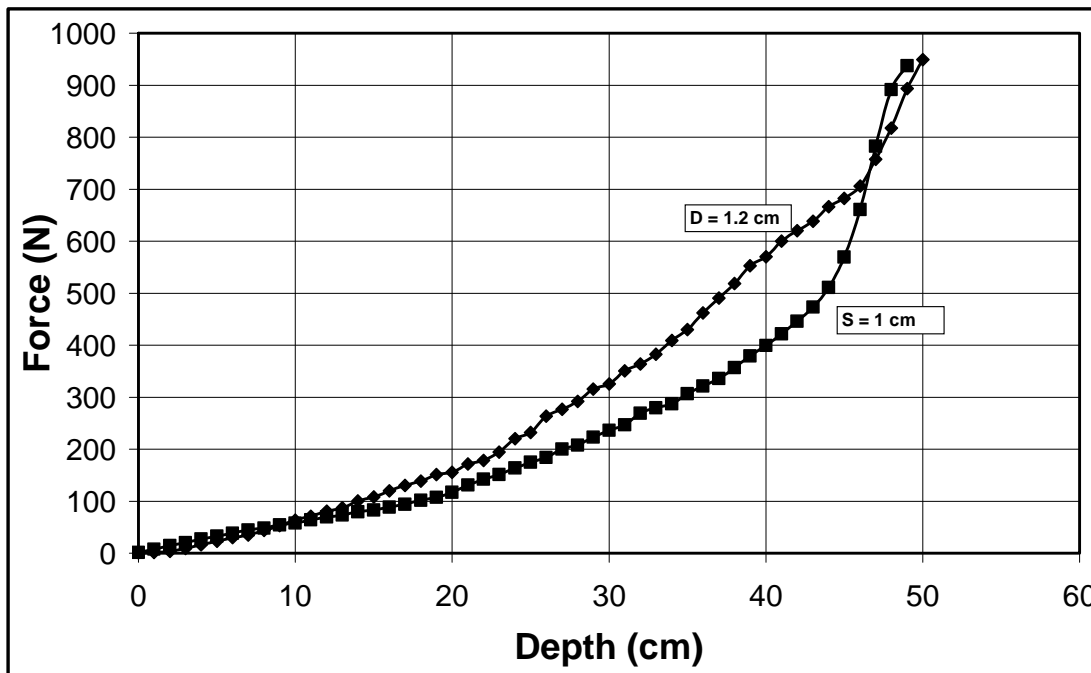


Figure 6.14. Penetration force as a function of depth in sand for two probe shapes (D = 1.2 cm, S = 1 cm, Tip angle is 30°, bulk density is 1700 kg/m³).

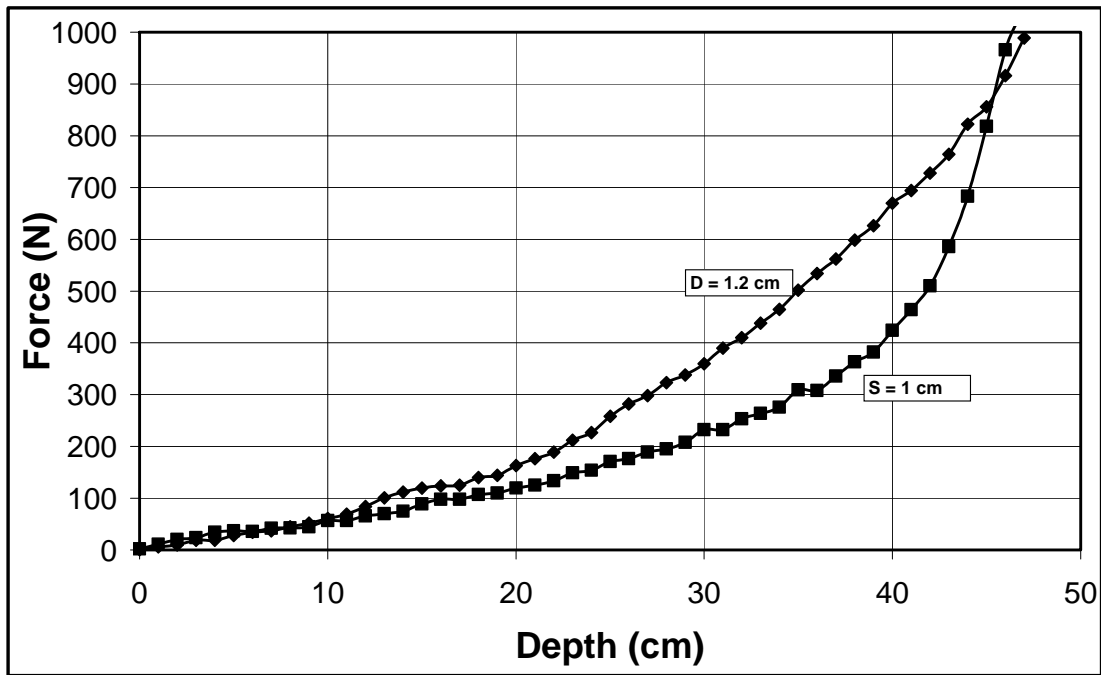


Figure 6.15. Penetration force as a function of depth in sand for two probe shapes (D = 1.2 cm, S = 1 cm, Tip angle is 60°, bulk density is 1700 kg/m³).

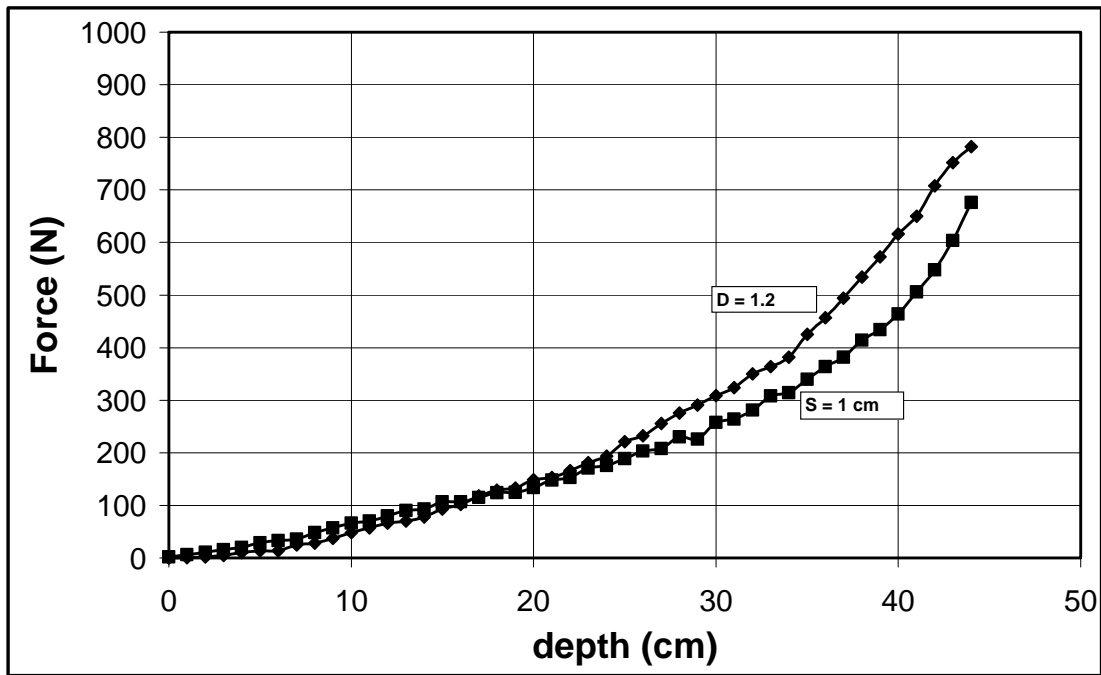


Figure 6.16. Penetration force as a function of depth in sand for two probe shapes (D = 1.2 cm, S = 1 cm, Tip angle is 90°, bulk density is 1700 kg/m³).

JSC Mars-1

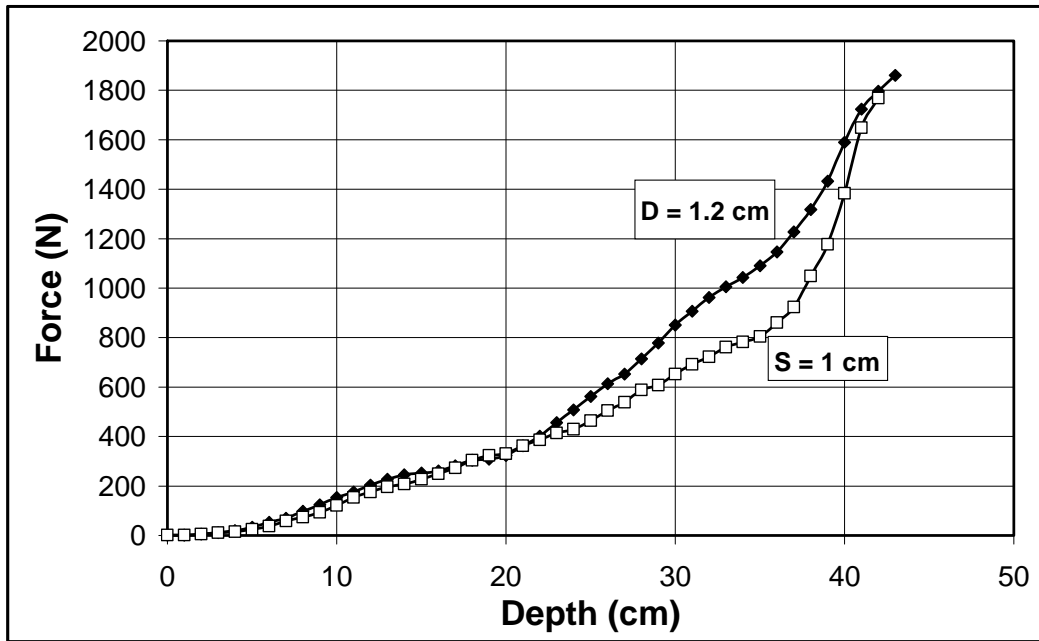


Figure 6.17. Penetration force as a function of depth in JSC Mars-1 for two probe shapes ($D = 1.2$ cm, $S = 1$ cm, Tip angle is 30° , bulk density is 1090 kg/m³).

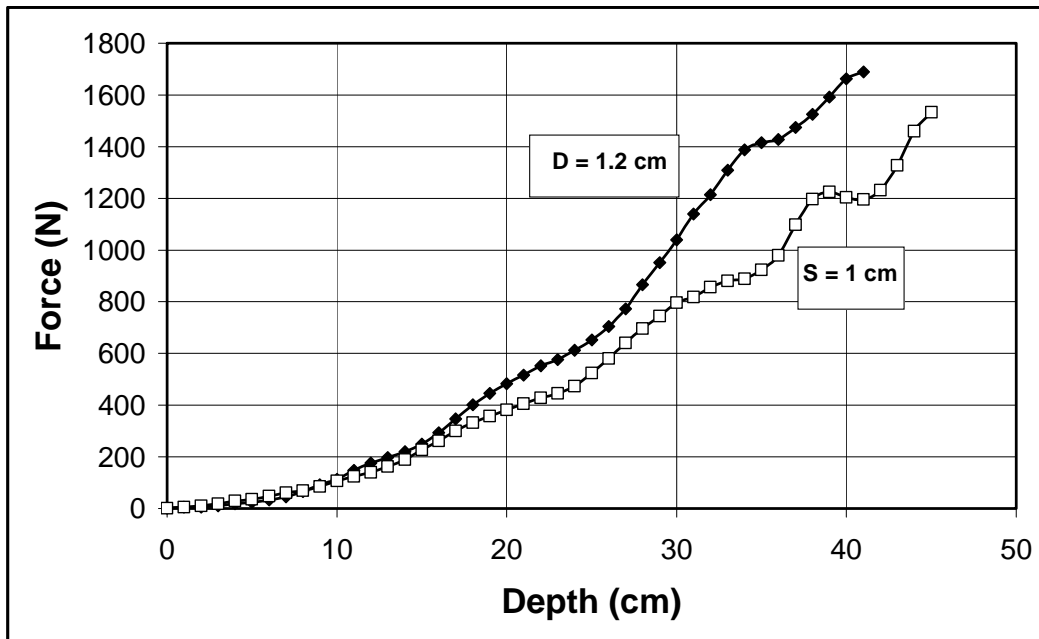


Figure 6.18. Penetration force as a function of depth in JSC Mars-1 for two probe shapes ($D = 1.2$ cm, $S = 1$ cm, Tip angle is 60° , bulk density is 1090 kg/m³).

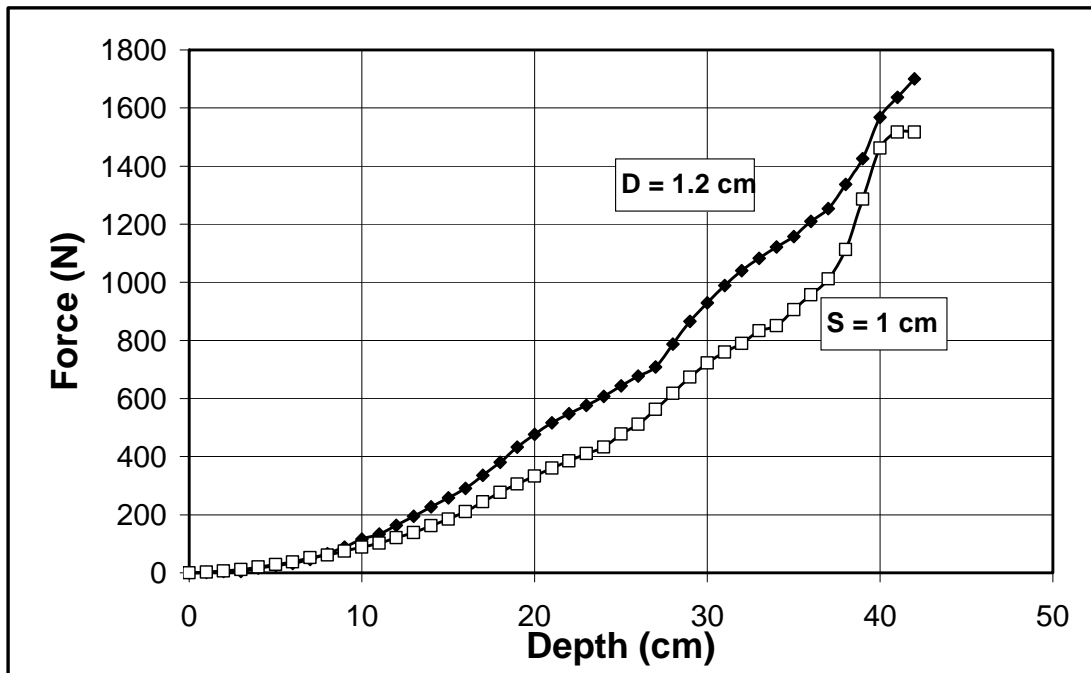


Figure 6.19. Penetration force as a function of depth in JSC Mars-1 for two probe shapes ($D = 1.2$ cm, $S = 1$ cm, Tip angle is 90° , bulk density is 1090 kg/m³).

JSC Mars-2

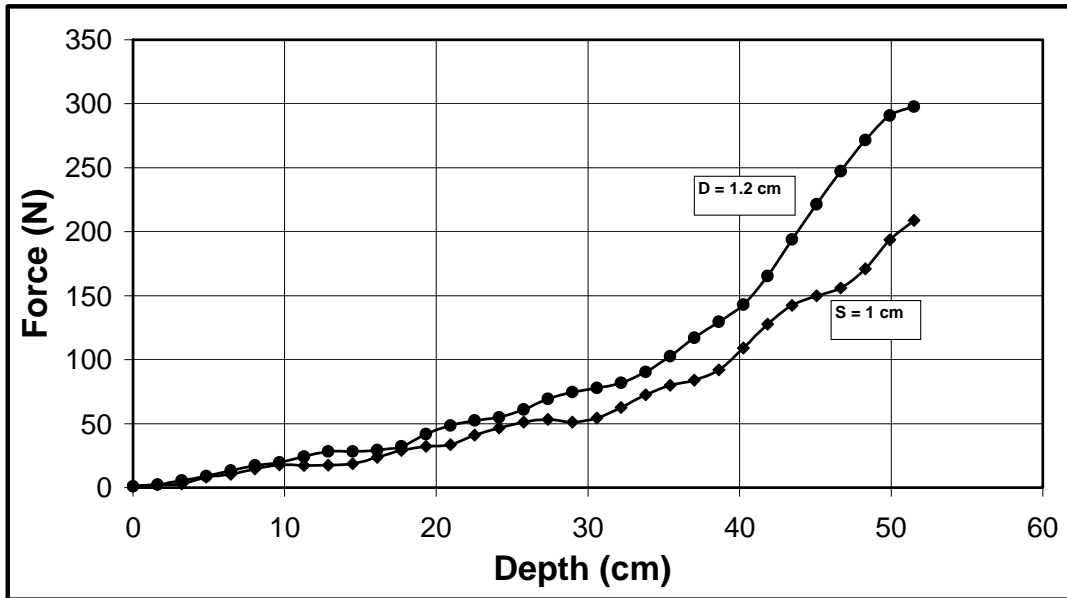


Figure 6.20. Penetration force as a function of depth in JSC Mars-2 for two probe shapes ($D = 1.2$ cm, $S = 1$ cm, Tip angle is 30° , bulk density is 1180 kg/m³).

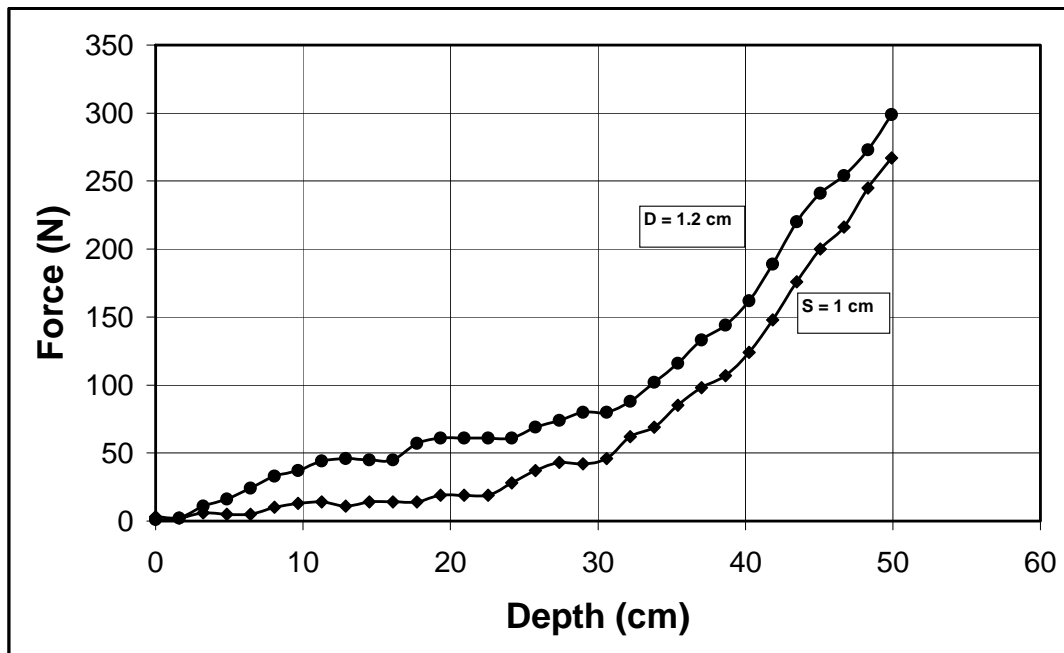


Figure 6.21. Penetration force as a function of depth in JSC Mars-2 for two probe shapes ($D = 1.2$ cm, $S = 1$ cm, Tip angle is 60° , bulk density is 1180 kg/m³).

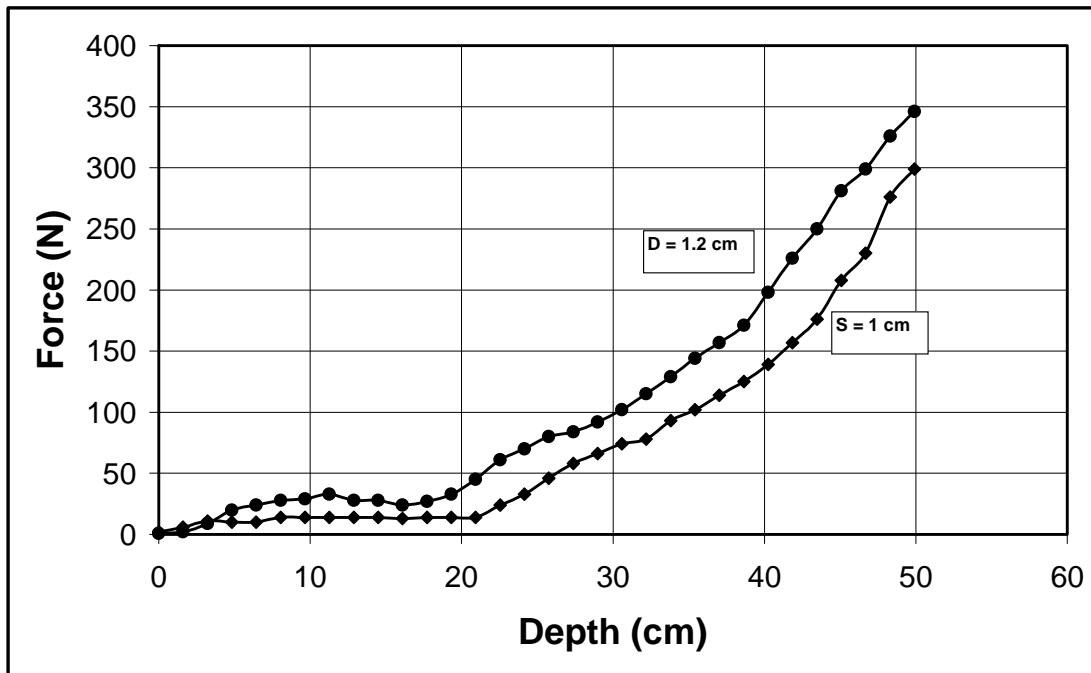


Figure 6.22. Penetration force as a function of depth in JSC Mars-2 for two probe shapes ($D = 1.2$ cm, $S = 1$ cm, Tip angle is 90° , bulk density is 1180 kg/m³).

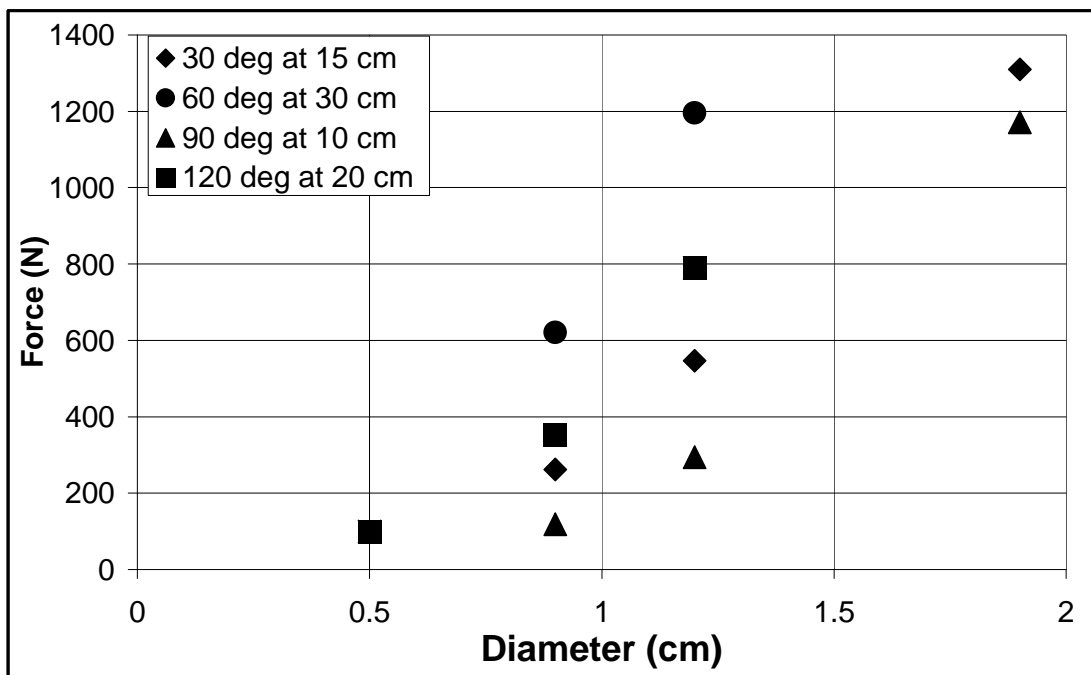


Figure 6.23. Variation of different diameter probes as a function of force.

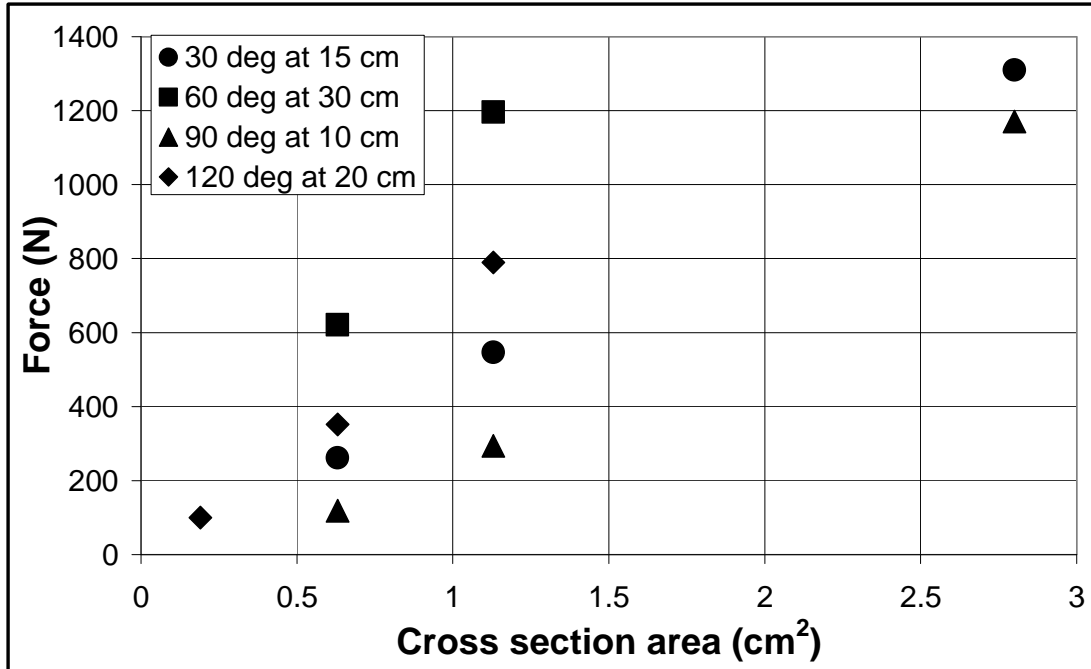


Figure 6.24. Variation of different cross section area of circular probe as a function of force.

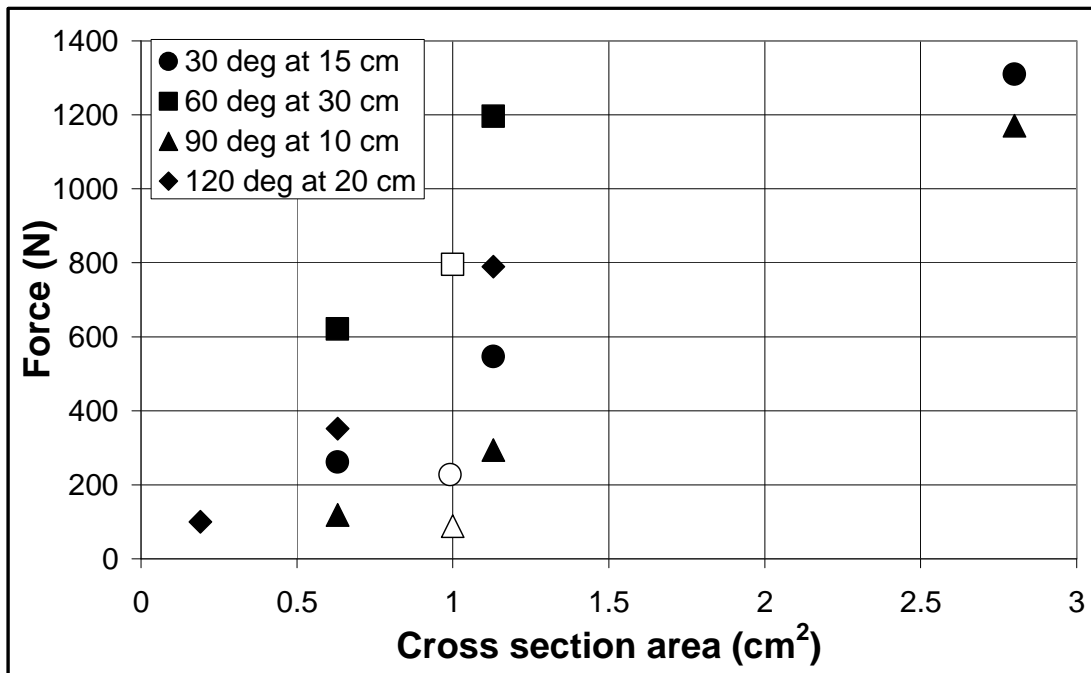


Figure 6.25. Variation of circular and square cross sectional areas as a function of force (white filling for square probes).

Cross section area shows somewhat more linearity with the insertion force as seen in Figure 6.25 than the diameter data (Figure 6.24). We do not have two probes (circular and square) with the same cross section area to compare but square probes show less force as can be seen in Figure 6.24. We did want to do least-square fit for the data in Figure 6.23, 6.24 and 6.25 to check the linearity but we were limited by the number of the data points. OPRA will have a square cross section in order to accommodate the need for flat windows.

6.5. Effect of Diameter

Five different circular probes were made with different diameters (2.5, 1.9, 1.2, 0.9 and 0.5 cm) are tested and the tip angle is fixed in each experiment. The tip angle was already shown to have little influence.

Sand

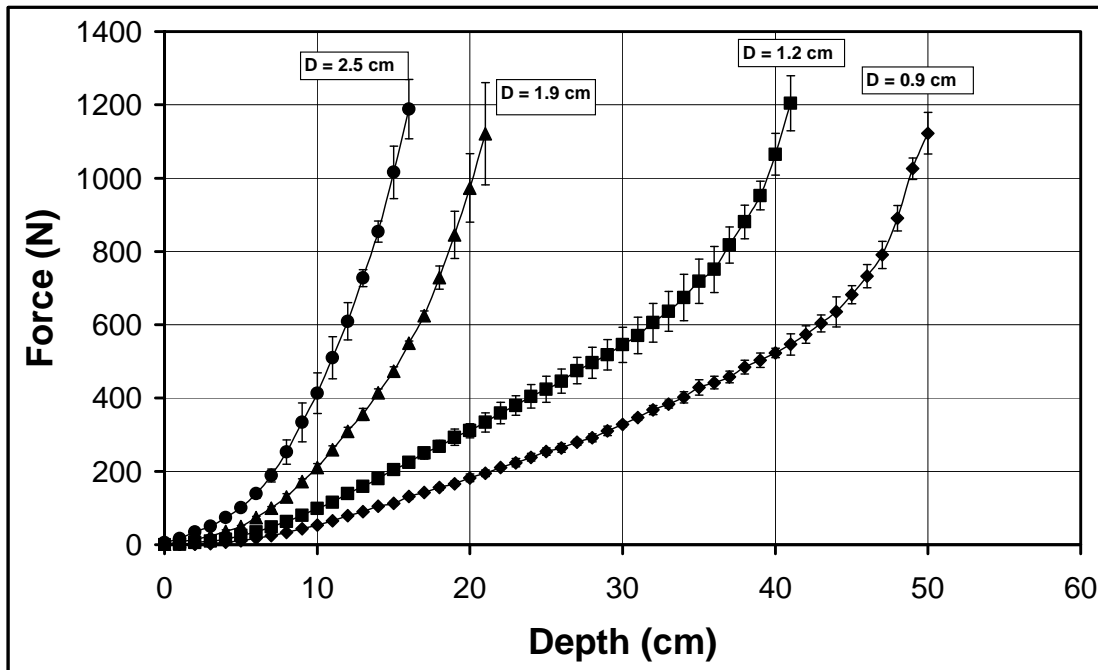


Figure 6.26. Penetration force as a function of depth in sand for different diameter probes (Tip angle is 30° ; bulk density is 1700 kg/m^3).

JSC Mars-1

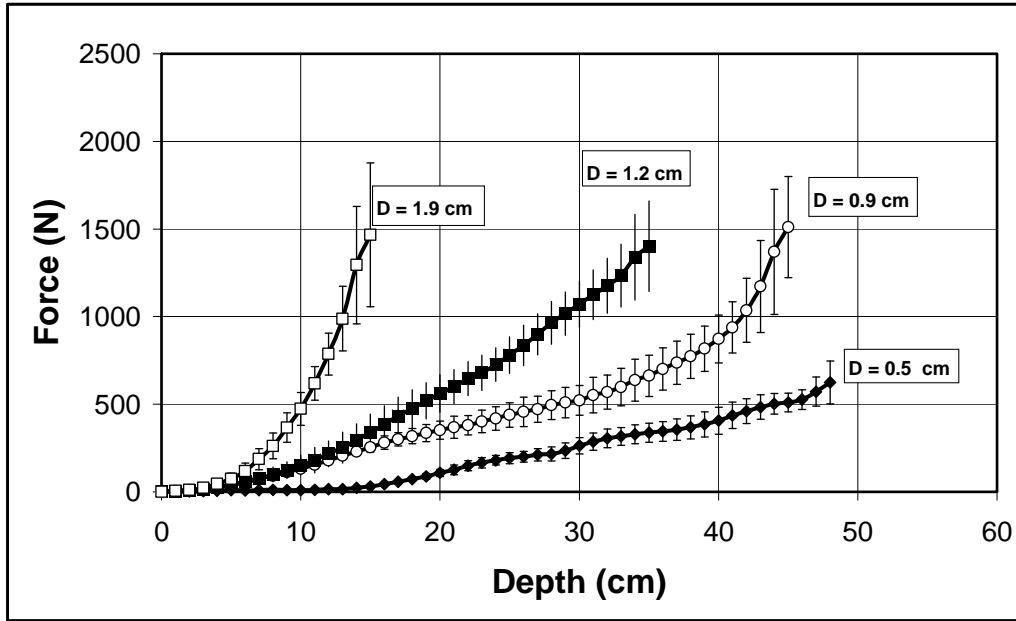


Figure 6.27. Penetration force as a function of depth in JSC Mars-1 for different diameter probes (Tip angle is 120° ; bulk density is 1090 kg/m^3).

JSC Mars-2

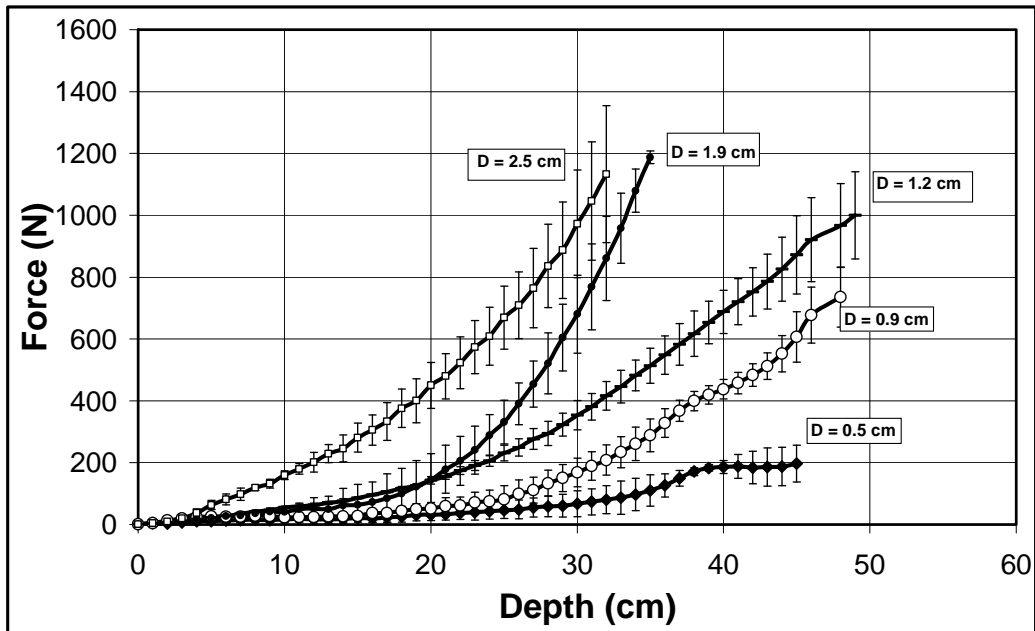


Figure 6.28. Penetration force as a function of depth in JSC Mars-1 for different diameter probes (Tip angle is 30° ; bulk density is 1180 kg/m^3).

Mojave soil

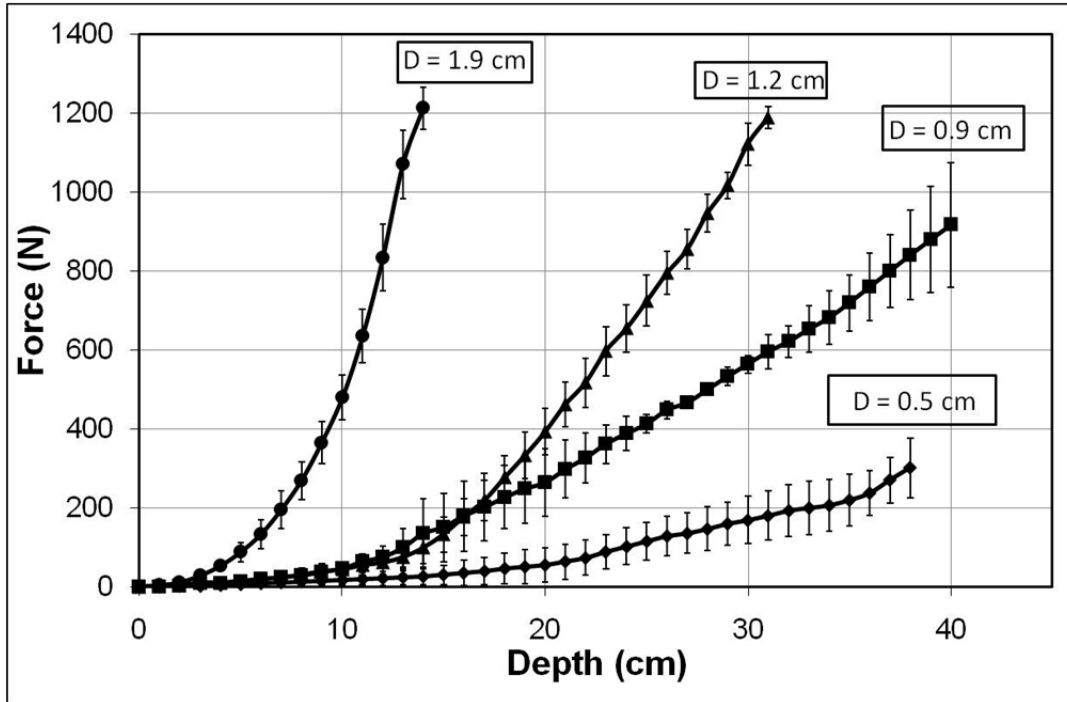


Figure 6.29. Penetration force as a function of depth in Mojave soil for different diameter probes (Tip angle is 60° bulk density is 1600 kg/m^3).

7. Discussion

7.1 Bearing Capacity Theory

Penetration into regolith material is resisted by two reaction forces from the subsurface; the force acts on the cone (cone resistance) and the force acts on lateral surface of the sleeve (sleeve friction). Bearing capacity is the capacity of the soil to support loads without being sheared (V. N. S. Murthy, 2002). The total resistance force (F_T) during probes insertion into the subsurface is the sum of two forces; force on cone (F_C) and force on sleeve (F_S).

$$F_T = F_C + F_S \quad (1)$$

Where

$$F_C = q_c A_c, \quad F_S = q_s A_s$$

Where,

F_T = total resistance force in (N)

F_C = force on cone in (N)

F_S = force on sleeve in (N)

q_c = cone resistance (Pa)

q_s = sleeve resistance (Pa)

A_s = area of the sleeve in (m^2), $A_s = 2\pi rz$, r is the radius of sleeve and z is the penetration depth.

A_c = area of the cone in (m^2), $A_c = \pi rs$, r is the radius of cone circle and s is the length of cone side

The cone resistance can be calculated from

$$q_c = \gamma \times z \times Nq \left(1 + \left(K \times \sin \phi \times \frac{z}{L} \right) \right) \quad (\text{Puech A., 2002}) \quad (2)$$

The sleeve resistance can be calculated from

$$q_s = \frac{Kp \times \gamma \times Z}{3} \quad (\text{Harr, 1977}) \quad (3)$$

Where,

γ = effective unit weight of sand (N/m³)

z = penetration depth (m)

ϕ = friction angle (degree), $\phi = 25 + (0.15 \times Dr)$ (M. E. Harr, 1977)

D_r = Relative density

K = coefficient of lateral pressure at rest (dimensionless), $K = 1 - \sin \phi$ (M. E. Harr, 1977)

Kp = the passive coefficient of lateral stress, $Kp = \frac{1 + \sin \phi}{1 - \sin \phi}$ (M. E. Harr, 1977)

Nq = bearing capacity factor (dimensionless), $Nq = 1.0584 \times e^{6.1679 \times \tan \phi}$

L = lateral extension of the slip lines (m), $L = B \times e^{\left(\frac{\pi}{2} \times \tan \phi\right)} \times \tan\left(\frac{\pi}{4} + \frac{\phi}{2}\right)$

B = cone diameter (m)

7.2 Procedure for determining q_c in sand:

7.2.1. Particle Density Measurements for Sand (ρ_s):

Particle density measurement for sand was carried out by filling a beaker with water to a specific volume (initial volume). A known mass of sand is poured inside the beaker which forces the water level to increase and reach to its final volume. The change in volume is calculated and the corresponding particle density is determined. Sand particle density found to be 2556 kg/m³.

7.2.2. Porosity (n)

Porosity is the ratio of the volume of voids to the total volume (V. N. S. Murthy, 2002). From the knowledge of particle density of sand and the bulk density, the porosity can be calculated from

$$n = 1 - \frac{B.D}{P.D} = \frac{V_v}{V} \quad (4)$$

Where

$B.D$ = bulk density of sand (kg/m^3)

$P.D$ = particle density of sand (kg/m^3)

V_v = volume of voids (m^3)

V = total volume (m^3)

7.2.3. Void Ratio (e)

Void ratio is the ratio between volumes of voids to volume of solids of certain material (V. N. S. Murthy, 2002).

$$e = \frac{V_v}{V_s} \quad (5)$$

The maximum and minimum void ratios correspond to the void ratio of sand in its loosest and densest state. From the knowledge of particle density of sand, the volume of solid particles can be calculated from

$$V_p = \frac{m_s}{\rho_s} \quad (6)$$

Where

V_p = volume of solid particles (m^3)

m_s = mass of sand (kg)

ρ_s = particle density of sand (kg/m^3)

The total volume of particles and voids (V_T) are measured separately in each case of loosest and densest state. From the volume of solid particles (V_p), the volume of voids (V_v) is calculated by

$$V_v = V_T - V_p$$

Therefore,

$$e_{\max} = \frac{V_{voids(max)}}{V_{solids(max)}} \quad , \quad e_{\min} = \frac{V_{voids(min)}}{V_{solids(min)}} \quad (7)$$

The maximum and minimum void ratios for sand are found to be 0.71 and 0.34 respectively.

7.2.4. Relative Density (D_r)

It is an index that quantifies the degree of compaction (packing between loosest and densest state) of coarse-grained soils (V. N. S. Murthy, 2002).

$$D_r = \frac{e_{\max} - e}{e_{\max} - e_{\min}} \quad (8)$$

Where

e_{\max} = is the maximum void ratio (loosest condition)

e_{\min} = is the minimum void ratio (densest condition)

e = current void ratio.

7.3 Theoretical Vs Experimental data:

We theoretically predicated the forces acting on the cone (F_c) and on the sleeve (F_s) using equations 2 and 3; and we added the two forces to predict the total penetration force (F_T) using

equation 1 (Figure 7.2). Table 7.1 shows the parameters used in our model and their corresponding values. Figure 7.1 shows the cone and sleeve resistance as presented in Pa where the effect of sleeve resistance is minimal compared to the forces acting up on the cone.

Table 7.1. Parameters used in the theoretical penetration model

Parameter	Value
Probe diameter	0.009 m
Bulk density	1700 kg/m ³
Particle density	2650 kg/m ³
Porosity	0.296
Void ratio	0.42
Maximum void ratio	0.71
Minimum void ratio	0.35
Relative density	80.5
Friction angle	37
coefficient of lateral pressure	0.39
passive coefficient of lateral stress	4
lateral extension of the slip lines	0.010 m
Effective unit weight	16677 N/m ³
Bearing capacity factor	93
Area of cone	0.000106 m ²
Area of sleeve	0.028 (0.0045 + z) m ²

Sleeve friction forces are observed to have lower forces compared forces acting up on the cone. At about 50 cm deep, sleeve friction force is about 25% of cone resistance. We observed a divergence between the model and the experimental data around 45 cm depth. After 45 cm, we are reaching the bottom of the cylinder and there is no place for the regolith to dilate which increase the resistance force, therefore, there is sharp increase in the experimental data after 45 cm depth.

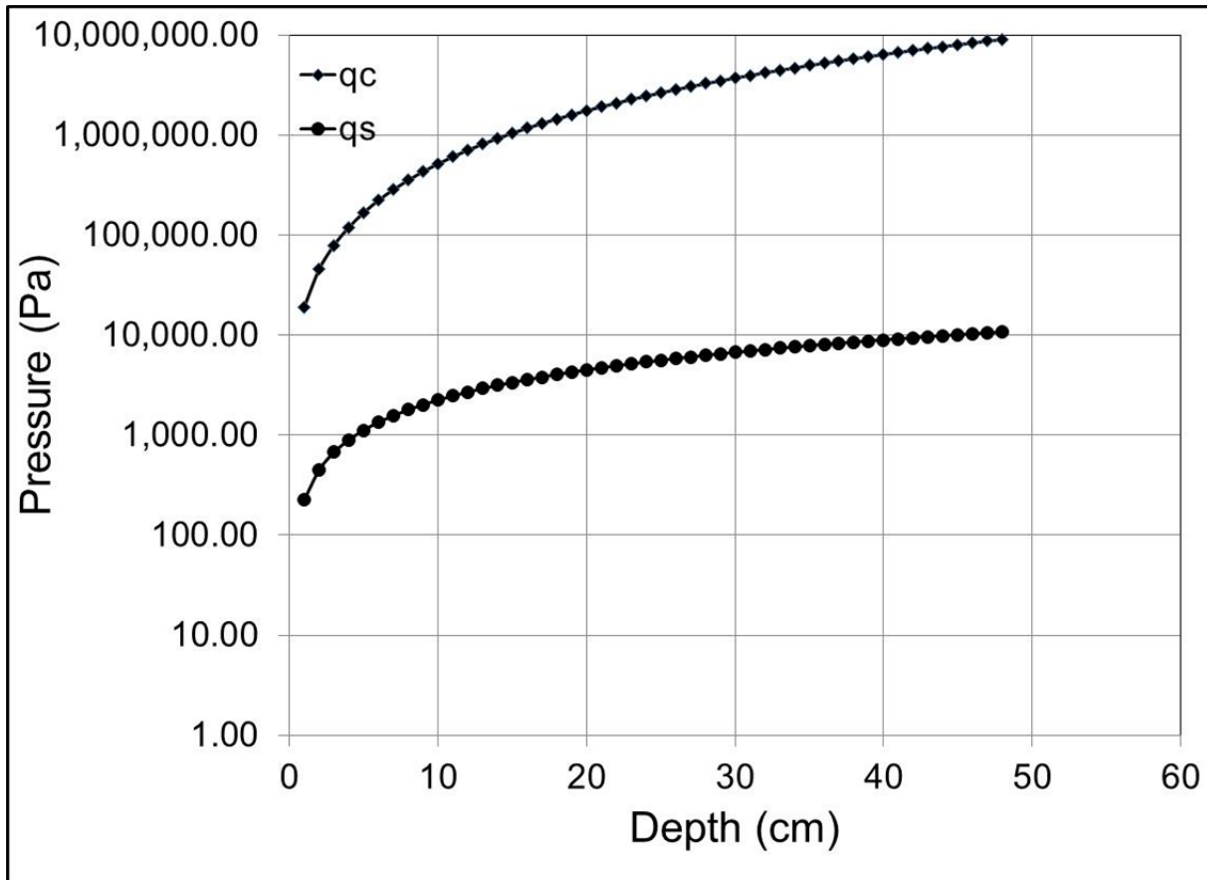


Figure 7.1. Theoretical cone and sleeve resistance in sand ($D = 0.9\text{cm}$, Bulk density = 1700 kg/m^3).

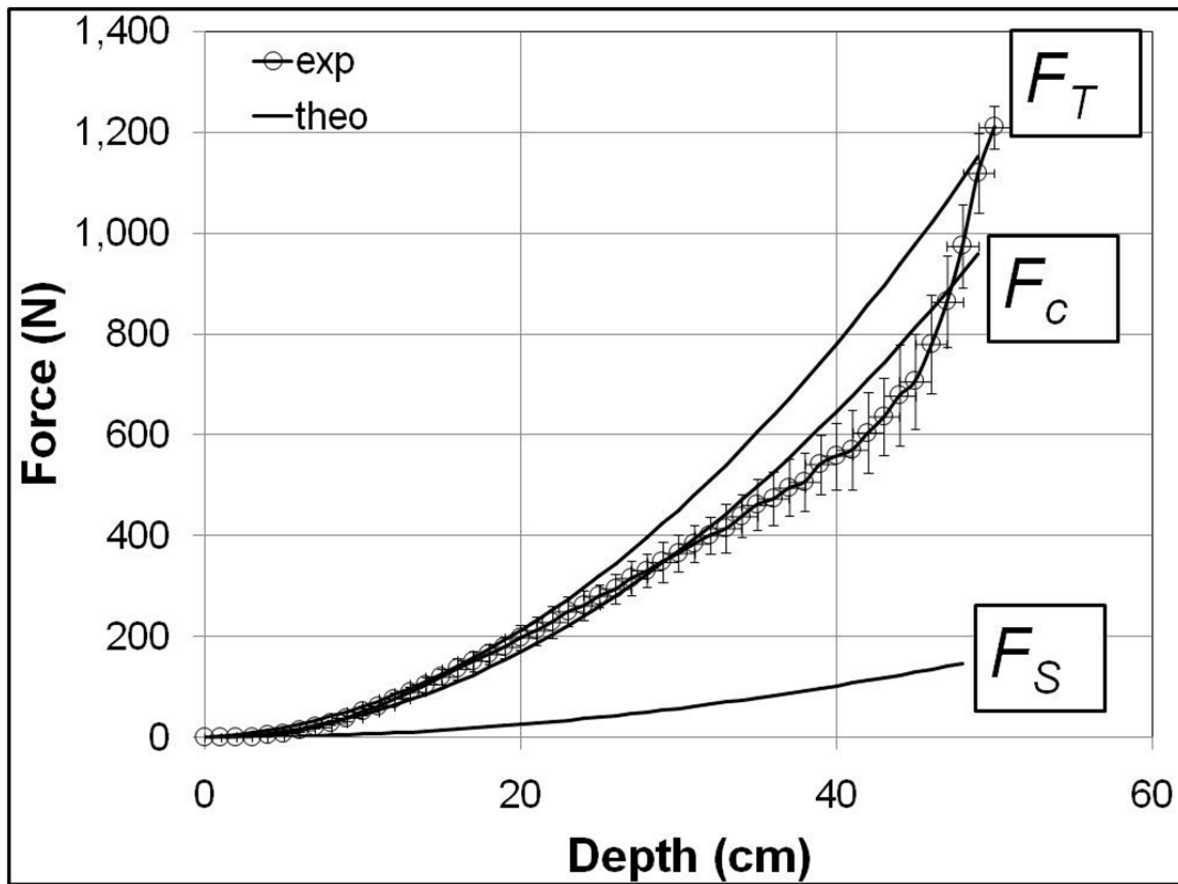


Figure 7.2. Theoretical versus experimental data in sand ($D = 0.9\text{cm}$, Bulk density = 1700 kg/m^3).

8. Conclusions

Different kinds of subsurface investigation instruments are now existed. Each has its advantages and disadvantages. Drills are a good choice for reaching great depth but it will destroy the formation and the structure of the subsurface. Besides, it will not be helpful for obtaining samples from the subsurface because the material is already mixed up and the samples are in an environment which is different than that was existed which may change its structure and composition. Impact penetrometers is best suited for low gravity planetary bodies such as asteroids and comets but it is a high risk instrument because during impact some of the inside instruments may be damaged, it may require some type of propulsion system to de-accelerate the penetrometer. On the other hand, if the impact penetrometer impacted in an angle other than vertical due to orientation in the atmosphere, reaching the desired depth is no longer an objective. Penetrometers and penetrators are considered as one of the most important and successful instruments which can be used to investigate the subsurface composition and structure of planetary bodies. It preserves the formation and can acquire samples simultaneously. The only constrain which affect the performance and efficiency of any kind of penetrometers or penetrators is the mass of the host planetary robot, rover and lander; and correspondingly the gravity of the target planet as well. Therefore, one of the most important conclusions which we can come out from this project is to estimate the amount of force needed to insert a probe down the sub-surface and the amount of force needed to pull it out from the subsurface of different planetary regolith analogs as a function of probes shape, length, tip angle and thickness under specific compaction level which we think it may resemble the condition on some of the planetary bodies.

It was found that by increasing the diameter of the probe, the corresponding penetration force increases linearly with depth. A tip angle does not show significance effect. In other words, no noticeable effect between a 30° tip and 120° tip. Regarding probes shape, we can conclude that the cross-sectional area is that matter, not the perimeter which affects the required insertion forces. The level of compaction is one of the most important factors which affect the penetration forces. These conclusions based on dry conditions of regolith, no consideration for icy soils is considered.

Mars Science Lab will be weighting about 3320 N on Mars; a 9 mm probe would be a good choice for a penetrometer to reach to about 0.5 m down the subsurface of Mars. Regarding the penetration power, Spirit and Opportunity each can generate a peak of about 150 W of solar power. Over an average sol with fairly clean panels, they can produce about 600 W-hrs of power, which is equal to 2.2 MJ. MSL will produce 125 W continuously from its radio-isotopic thermal generator, giving up to 3000 W-hrs/sol or 10.8 MJ. Our measurements in compacted Mars simulant with 0.9 cm diameter probe indicate a requirement of 200 J to achieve 0.5 m. The peak rate of required power for probe insertion will be only about 1.6 W (800 N times 0.002 m/s).

9. References

Alain Puech, FugroFrance; Pierre Foray, Institut National Polytechnique de Grenoble, *Offshore Technology Conference*, 6 May-9 May 2002, Houston, Texas, 2002.

Cherkasov, Il, V.V. Shvarev. Soviet investigations of the mechanics of lunar soils.1973. *Soil Mechanics and Foundation Engineering*, Springer Volume 10, Number 4 (1973), 252-256.

David L. Glaser, Andrew J. Ball, and Kris A. Zacny. A review of penetrometers for subsurface access on comets and asteroids. *Meteoritics & Planetary Science* 43, Nr 6, 1021–1032 (2008)

Gromov V. V., Mischevich A. V., Yudkin E. N., Kochan H., Coste P., and Re E. 1997. The mobile penetrometer, a “mole” for subsurface soil investigation. *Proceedings, 7th European Space Mechanisms and Tribology Symposium, ESTEC*, Noordwijk, The Netherlands, 1–3 October, 1997. ESA Special Publication- 410. pp. 151–156.

Harr M. E., *Mechanics of particulate media*. McGraw-Hill, 1977, P.260.

Jones A. P., Pickering K. T., 2003, Evidence for aqueous fluid–sediment transport and erosional processes on Venus, *Journal of the Geological Society*, London, Vol. 160, 2003, pp. 319–327.

Kerr R. A. 2005. Deep Impact finds a flying snowbank of a comet. *Science* 309:1667.

Kochan H., Hamacher H., Richter L., Hirschmann L., Assanelli S., Nadalini R., Pinna S., Gromov V. V., Matrossov S., Yudkin E. N., Coste P., Pillinger C., and Sims M. 2001. The Mobile Penetrometer (Mole)—A tool for planetary sub- surface investigations. In *Penetrometry in the solar system*, edited by Kömle N., I., Kargl G., Ball A. J., and Lorenz R. D. Graz, Austria: Space Research Institute, *Austrian Academy of Sciences*. pp. 212–243.

Leonovich, AK, VV Gromov, AD Dmitriev, VA Lozhkin, VN Penetrigov, PS Semionov, IN Grannik, VP Grushevskii, and VV Shvarev. 1976. Investigation of the physical and mechanical properties of the lunar sample brought by luna-20 and along the route of motion of lunokhod 2. In: *Space Activity Impact on Science and Technology. (A76-35711 17-12)* Oxford, Pergamon Press, Ltd., 1976, p.321-332. 1 : 321-32.

Leonovich, AK, VV Gromov, AV Rybakov, VN Petrov, PS Pavlov, II Cherkasov, and VV Shvarev. 1972. Investigations of the mechanical properties of the lunar soil along the path of lunokhod 1. Paper presented at Space Research.

Longwell & Flint, *Introduction to Physical Geology*, 1962, p.324-345

Lorenz R. D., Bannister M., Daniell P. M., Kryszinski Z., Leese M. R., Miller R. J., Newton G., Rabbett P., Willett D. M., and Zarnecki J. C. 1994. An impact penetrometer for a landing spacecraft. *Measurement Science and Technology* 5:1033–1041.

Malin, M.C. & Edgett, K.S. 2000a. . Sedimentary rocks of early Mars. *Science*, 290, 1927–1937.

Mitchell, J.K., W.N. Houston, W.D. Carrier and N.C. Costes. 1974. Apollo soil mechanics experiment S-200. Final report, NASA Contract NAS 9-11266, *Space Science Laboratory Series 15*, Issue 7, Uni. California, Berkeley.

Murthy V. N. S. Geotechnical Engineering: Principles and Practices of Soil Mechanics and Foundation Engineering (Civil and Environmental Engineering). *CRC*, 2002.

Pilgrim, R., R. Ulrich. 2012. Numerical modelling and optimization of bundled fiber optic FTIR probes for spectroscopy of small targets. *Advances in Space Research*. Volume 49, Issue 4, Pages 621-628.

Pinna S., Angrilli F., Kochan H., and Richter L. 2001a. Development of the mobile penetrometer (mole) as sampling tool for the Beagle 2 Lander on Mars Express 2003. *Advances in Space Research* 28:1231–1236.

Richter L., Coste P., Gromov V. V., Kochan H., Nadalini R., Ng T. C., Pinna S., Richter H.-E., and Yung K. L. 2002. Development and testing of subsurface sampling devices for the Beagle 2 Lander. *Planetary and Space Science* 50:903–913.

Richter L., Coste P., Gromov V. V., Grzesik A., 2004. The mole with sampling mechanism (MSM)—Technology development and payload of beagle 2 mars lander *Proceedings, 8th ESA Workshop on Advanced Space Technologies*

Spencer, Physical Geology, 1983, P.77-78.

Stoker¹, L. Richter, W.H. Smith, L.G. Lemke, P. Hammer, J.B. Dalton, B. Glass and A. Zent. The Mars underground mole (MUM): a subsurface penetration device with insitu infrared reflectance and raman spectroscopic sensing capability. *Sixth International Conference on Mars* (2003).

Squyres, Steven W., Andrew H. Knoll, Raymond E. Arvidson, James W. Ashley, James F. III Bell, Wendy M. Calvin, Philip R. Christensen, et al. 2009. Exploration of Victoria Crater by the Mars rover Opportunity. *Science* 324(5930): 1058-1061.

Strahler, Physical Geology, 1981, P.165-166

Veveřka J., Farquhar B., Robinson M., Thomas P., Murchie S., Harch A., Antreasian P. G., Chesley S. R., Miller J. K., Owen W. M. Jr, Williams B. G., Yeomans D., Dunham D., Heyler G., Holdridge M., Nelson R. L., Whittenburg K. E., Ray J. C., Carcich B., Cheng A., Chapman C., Bell J. F. III, Bell M., Bussey B., Clark B., Domingue D., Gaffey M. J., Hawkins E., Izenberg N., Joseph J., Kirk R., Lucey P., Malin M., McFadden L., Merline W. J., Peterson C.,

Prockter L., Warren J., and Wellnitz D. 2001. The landing of the NEAR Shoemaker spacecraft on asteroid 433 Eros. *Nature* 6854:390–393.

Zarnecki J. C., Leese M. R., Hathi B., Ball A. J., Hagermann A., Towner M. C., Lorenz R. D., McDonnell J. A. M., Green S. F., Patel M. R., Ringrose T. J., Rosenberg P. D., Atkinson K. R., Paton M. D., Banaszkiwicz M., Clark B. C., Ferri F., Fulchignoni M., Ghafoor N. A. L., Kargl G., Svedhem H., Delderfield J., Grande M., Parker D. J., Challenor P. G., and Geake J. E. 2005. A soft solid surface on Titan as revealed by the Huygens surface science package. *Nature* 438:792–795.